D5.1 - Definition of materials and manufacturing procedure for the submerged polymeric PTO

DATE: October 2016

PROJECT COORDINATOR:
WavEC Offshore Renewables

GRANT AGREEMENT NR: 646436
PROJECT: WETFEET

The WETFEET – Wave Energy Transition to Future by Evolution of Engineering and Technology project has received funding from the European Union's Horizon 2020 programme under grant agreement No 641334.

Report on the definition of materials and manufacturing procedure for the submerged polymeric PTO			
Project	WETFEET – Wave Energy Transition to Future by Evolution of Engineering and Technology		
WP No.	5	WP Title	Submerged Polymeric PTO Breakthrough
Deliverable No.		5.1	
Nature (R: *Report*, P: *Prototype*, O: *Other*)		R	
Dissemination level (PU, PP, RE, CO)		PU	
Lead beneficiary:		JKUL	
Contributing partners		SSSA, JKUL	
Authors List:		Marco Fontana, Giacomo Moretti, Siegfried Bauer, Rainer Kaltseis	
Quality reviewer		José Cândido	
Status (F: final; D: draft; RD: revised draft):		F	
Due Delivery Date:		31/10/2016	
Actual Delivery Date:		31/01/2016	

Version no.	Dates and comments
1	7 July 2016, definition of the preliminary structure of the report
2	20 September 2016 - First draft material
3	4 October 2016 – Second Draft
4	27 October – Complete Draft
5	31 October – Final version

Table of Contents

Table of figures

Table of tables

EXECUTIVE SUMMARY

This deliverable reports on a set of experimental tests that has been conducted within the framework of Workpackage 5 (WP5) of the WETFEET Project. Specifically, this WP is focused on Dielectric Elastomer Generators (DEG), i.e. a completely new technology for the conversion of mechanical energy into electrical energy that makes use of elastomeric-made variable capacitor.

These devices have demonstrated their potential for implementation of effective the Power Take Off (PTO) systems of a Wave Energy Converter (WEC). However, given their early stage of engineering development several aspects have still to be investigated.

Several key material properties of elastomeric materials that are employed for implementation of this PTO have been analysed in the past but further aspects were still to be analysed such as leakage losses due to residual conductivity of insulators, joule losses due to residual resistivity of conducting materials, and possible detrimental effect on material properties due to water contact.

In the first phase of the activities of WP5 (Task 1), the focus was set on the study on those aspect of material choice and combination that were not previously investigated. Specifically, a comprehensive study on the insulation properties of dielectric materials and the conductivity of materials employed for electrodes have been introduced. The most promising materials have been considered for the dielectrics (acrylic elastomers, natural and synthetic rubbers) and electrodes (filled PDMS, crumpled metalized electrodes).

Absolute values for conductivity have been measured and preliminary projections have been made in order to understand the effect of these properties on real scale devices.

It has been concluded that materials such as silicone and rubbers possess the insulation qualities to be employed has dielectric materials for DEGs. Acrylic elastomer are less reliable and presents high batch to batch variability. This could be attributable to manufacturing issues. Actually, material films that are tested are mostly conceived for completely different applications and their performance could be improved by assuming tailor-made manufacturing procedures. For what concern materials for electrode it has been found that solutions that employs composite silicone-carbon black materials can achieve a sufficient level of conductivity, i.e. the power loss during the required charging and discharging cycles are estimated to be well below 1%.

In parallel, a first set of tests have been initiated to characterize the behaviour of insulation layers in presence of direct contact with water. In this framework, materials are tested in direct contact interaction, i.e. the dielectric is put in contact with water showing important performance degradation. In a second set of studies, the effect of passivation barriers is investigated as a mean of mitigation of such degradation. Promising results that lead to significant improvements are obtained using dielectric barriers and hydrogel electrodes.

Additionally, in this report a first analysis is provided on manufacturability of full scale DEG main components. A general layout/architecture for the full scale DEG-PTO is proposed according to a modular structure. Possible existing manufacturing technologies are identified for the development of full-scale systems up to a scale of tens of kilowatts. However, the need of innovative manufacturing technologies is also identified for the development of larger scale systems.

LIST OF ACCRONYMS

CAPEX	Capital Expenditures
CD-DEG	Circular Diaphragm Dielectric Elastomer Generator
DE	Dielectric Elastomers
DEG	Dielectric Elastomer Generator (to refer to the whole generator)
EAM	Enhanced Added-Mass
EHC	Energy Harvesting Cycle (to refer to a single working cycle of a DEG)
LCOE	Levelized Cost of Electricity
NS	Negative Spring
OPEX	Operational Expenditures
OWC	Oscillating Water Column
PDE	Partial Differential Equation
PTO	Power Take-Off
TRL	Technology Readiness Level
TPL	Technology Performance Level
WEC	Wave Energy Converter

1. INTRODUCTION

1.1 Dielectric elastomer generators

Dielectric Elastomer Generators (DEGs) are a promising technology that could provide the breakthrough required by the wave energy sector [10].
DEGs are highly deformable capacitors (with deformations over 100%), made by elastomeric dielectric membranes coated with compliant electrodes (Fig.3), which can be used to convert mechanical energy into electricity and vice-versa. They operate via the variable capacitance electrostatic generation principle, thereby increasing the voltage of the charges that lie on DEG electrodes as the deformation in area of the DEG decreases [12].
The potential advantages of DEGs over conventional and competing technologies are: large energy densities (100-700J/kg); direct-drive and cyclic operation; good and rate-independent efficiencies (30-80%); moderate/low cost (5-15€/kg); good shock and corrosion resistance; easy manufacturability, deployment and disposal; silent operation; solid-state embodiment with self-sensing capabilities.

1.2 State-of-the art of DEG for wave energy conversion

Following the pioneering attempt by SRI International in collaboration with the Japanese HyperDrive Corp., current projects/companies that are working on DEGs for wave energy harvesting are: the FP7 PolyWEC and the H2020 WETFEET projects funded by the European Commission; the Eposil project funded by the German Federal Ministry of Education and Research; the SEASEA project funded by the French National Research Agency; the companies Bosch, SBM Offshore, Parker Hannifin, Wacker Chemie. The first three projects are coordinated and participated by the investigators of this new project.
Among all the DEG-based WEC concepts developed so far, the most architecture that has been considered as the most promising for first developments is the Polymeric Oscillating Water Column (Poly-OWC), whose concept has been conceived and validated within the PolyWEC project [12-19].

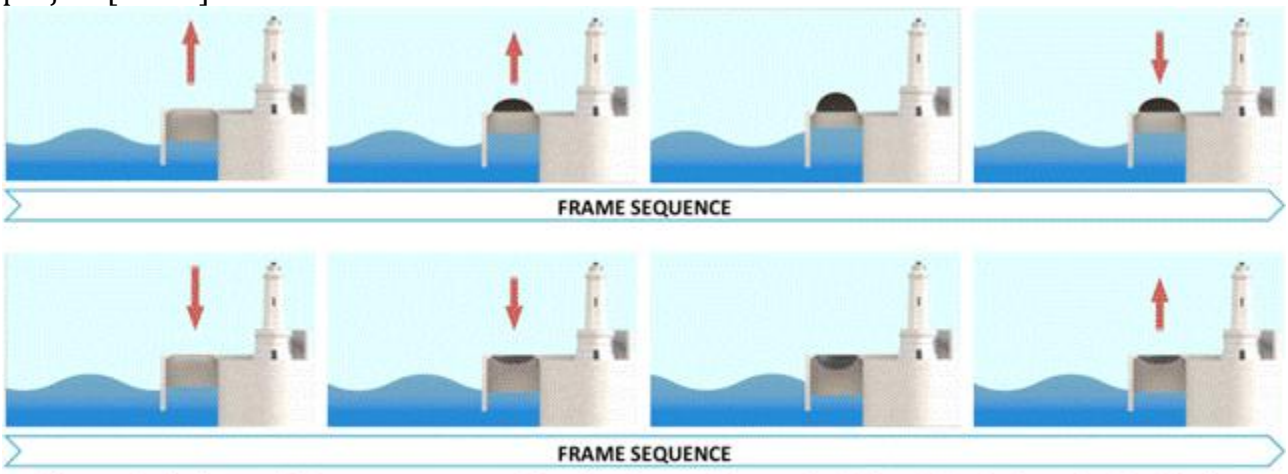

FIGURE 1-1. FRAME SEQUENCE ILLUSTRATING THE CONCEPT OF THE POLYOWC WAVE ENERGY CONVERTER

As depicted in Fig. 1-1, a Poly-OWC device features a semi-submerged hollow structure (namely, the OWC collector), open at the sea bottom to the incoming wave field and closed at

the top by a Circular Diaphragm DEG (CD-DEG). The Poly-OWC is filled in part with water (namely, the water column) and in part with air. As the waves impinge on the collector, the water column is put into reciprocating motion, which causes compression-expansion of the entrapped air and the resulting inflation-deflation of the CD-DEG. By properly charging and discharging the CD-DEG during its cyclical deformation, the Poly-OWC enables the conversion of ocean wave energy into electricity.

The Poly-OWC is an alternative version of traditional OWC concepts, that is probably the most studied and the best developed of all WEC systems, in which all the power conversion train (including turbine, electromagnetic generator, variable-speed drive and step-up transformer) is replaced by a single CD-DEG accompanied by a simple bi-directional capacitor charging/discharging electronics. In terms of the Technological Readiness Level (TRL), the Poly-OWC concept can currently be classified as TRL3 – "Initial Product Verification" (STAGE 1 – "Concept Validation"); that is, initial concept verification with 1:100 to 1:25 scale laboratory testing.

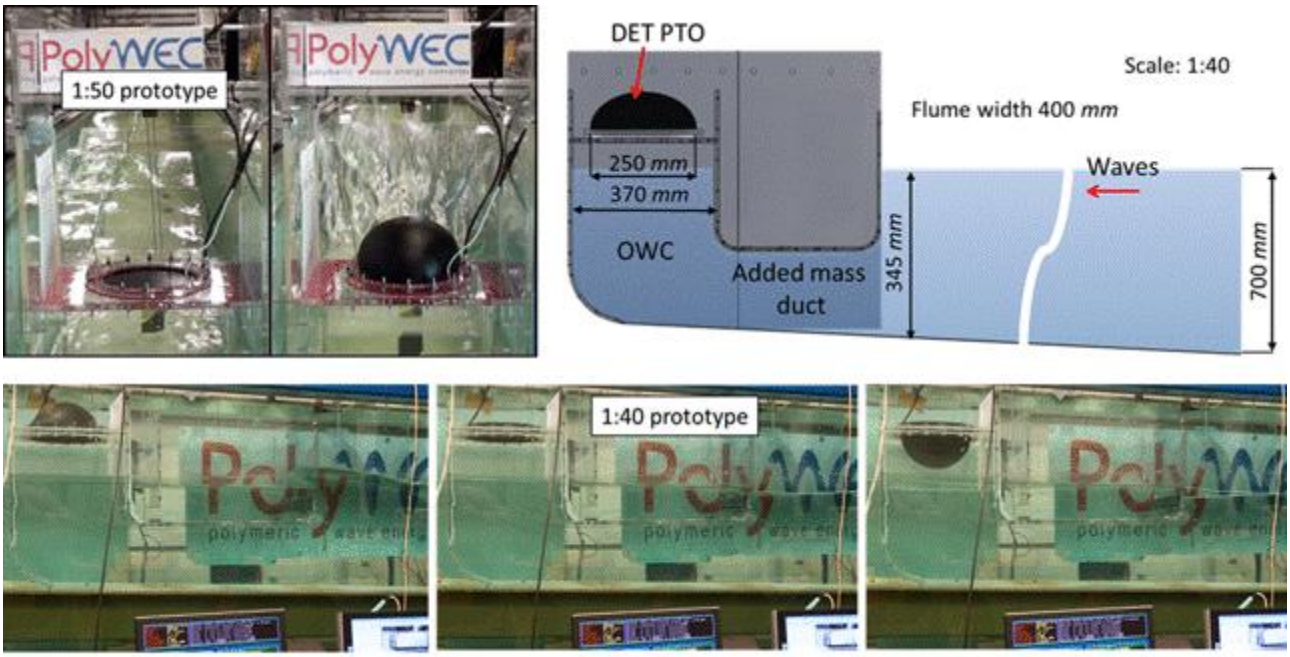

FIGURE 1-2. WAVE-TANK TEST OF 1:50 AND 1:40 SCALE POLYOWC PROTOTYPES.

Specifically, the following activities have been completed [12-19]:

- Identification and experimental characterization of materials for the construction of the DEG-PTO.
- Poly-OWC analysis, design and optimization via experimentally-validated numerical time-domain wave-to-wire simulation models (that include OWC hydrodynamics, DEG-PTO electro-hyperelasticity and energy harvesting electronics and control laws).
- Experimental evaluation of the power production with 1:50 and 1:40 scale fully-functional prototypes tested in wave tanks (Fig. 1-2). Results have been used to validate the simulation models mentioned above.
- Full-scale DEG-PTO defined. Hardware-in-the-loop (HIL) dry-run testing of 1:75 scale representative DET-PTOs in conjunction with the use of simulations to extrapolate to full-scale behaviour as well as to assess energy conversion efficiency and maximal control force capability (Fig. 1-3).

- Preliminary qualitative assessment of survival aspects with a 1:75 scale fully-functional prototype tested in a laboratory test-bench and with a 1:50 scale prototype tested in a wave flume with extreme wave conditions.
- Preliminary assessment of construction feasibility.
- Preliminary assessment via properly predisposed techno-economic (LCOE) and Carbon footprint (CO2e) models.

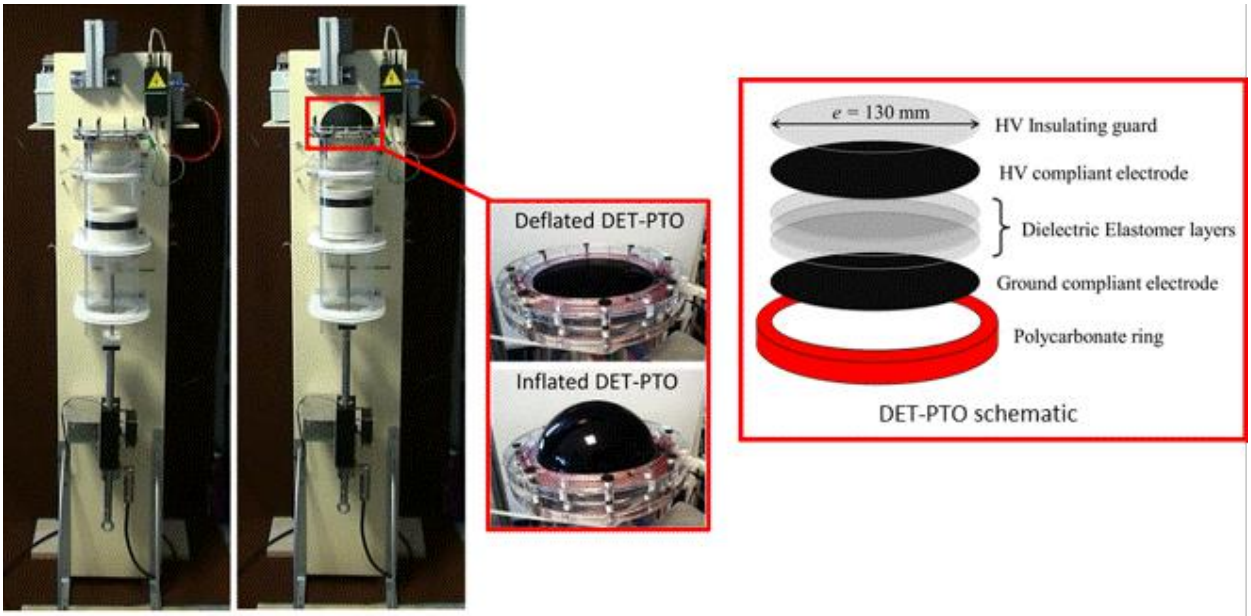

FIGURE 1-3. HARDWARE IN THE LOOP LABORATORY TESTS OF 1:75 SCALE DEG PTO PROTOTYPES.

1.3 DEG developments within WETFEET project

In the context of the WETFEET project, it is foreseen to go beyond the current state of the research and the PolyOWC concept. Specifically, the work is still focused on Circular Inflated DEG but the following main further developments are foreseen: (1) the further improvements of models through experimental campaign on materials; (2) the study of fully integrated control system and the testing on a larger scale hardware in the loop laboratory setup; (3) the study of the integration of DEG in different WEC architectures such as Spar Buoy and Symphony that can also include fully; (4) the study of submerged DEG that are in direct contact with sea water.

In the following sections the focus is set on research on materials for the development of DEGs. In the second section of this deliverable, an in depth analysis of dielectric and conductive deformable material properties is provided. The objective of this analysis is to provide numerical evaluation of the impact of key material-properties that were not previously analysed such as conductivity of dielectrics and resistivity of electrodes.

In the third section a first experimental analysis of DEGs in direct contact with water is provided. At first, experiments are conducted to verify/evaluate the decay of the key materials properties of dielectric material in presence of direct contact with water. In a second stage, solutions are elaborated and tested to block/mitigate the negative effects on the performances of materials.

In the fourth section a preliminary analysis is provided on manufacturability of full scale DEG main components. A general layout/architecture for the full scale DEG-PTO is proposed according to a modular structure. Possible existing manufacturing technologies are identified for the development of full-scale systems up to a scale of tens of kilowatts. However, the need of innovative manufacturing technologies is also identified for the development of larger scale systems.

2. ANALYSIS OF LOSSES

This section presents the experimental work that has been conducted in the framework of WP5 which aims at accurately characterizing the main sources of efficiency losses due to material properties. The results of experiments/measurements are described and mathematical models of dissipation mechanisms involved in DEGs operation are developed and employed to provide design considerations and materials choices.
Two fundamentals loss mechanisms have been identified:

- Leakage current losses, due to the non-ideal dielectric behaviour of the DE material, which exhibits a non-null electrical conductivity. Leakage currents affect the DEG operation throughout the whole generation cycle, as they tend to discharge the DEG. These losses are compensated by the external conditioning electronics, which is thus required to spend a certain amount of energy to maintain the established voltage on the DEG, preventing its discharge.
- Electrodes resistivity losses, due to the non-null resistivity of compliant electrodes. These losses might play a crucial role during DEG charging/discharging. Established DEG PTOs control strategies require indeed very fast charging/discharging of the DEG [1]. During these operations, series-resistances on the DEG might provoke large dissipations due to the fast R-C dynamics of the electrode-dielectric assembly. The effect of these losses can be mitigated either by using low-resistance compliant electrodes (compatibly with available materials) or limiting the maximum charging/discharging currents (compatibly with the timing of the generation cycle).

Experiments have been carried out in order to measure relevant physical constants describing the dissipation mechanisms, namely

- DE materials conductivity, and their dependence on the applied electric field;
- Sheet resistance of compliant electrodes samples, as a measure of their conductivity.

Mathematical models have been established, which use the abovementioned parameters to assess the effect of losses on hypothetic full-scale DEG PTOs and to set thresholds for material properties specifications. Theoretical analyses on both leakage and electrode losses make reference to a specific DEG architecture, namely Circular Diaphragm DEG (CD-DEG), which appears to be suitable for both in-air or submerged operation and is the main DEG architecture investigated within the Project.

2.1 Circular Diaphragm DEG

In this section, CD-DEG features and model are recalled. The aim of this section is providing a background of equations to enable successive implementations of losses models on this specific DEG architecture.

A CD-DEG is depicted in Figure 2-1. It consists of an equi-biaxially pre-stretched planar circular DE membrane that is clamped along its perimeter to a fixed frame at radius e and with thickness t (whereas e_0 and t_0 indicate the radius and thickness of the DEG in its planar undeformed state). The ratio between the frame radius, e, and the membrane undeformed radius, e_0, is referred to as pre-stretch: $\lambda_p=e/e_0$. The DEG in undeformed and pre-stretched configuration are shown in Figure 2-1(a) and Figure 2-1(b) respectively. In order to limit the applied voltage and to make the electric field within the generator more homogeneous, the

membrane can be split in a stack of parallel connected membranes, each coated by a couple of compliant electrodes.

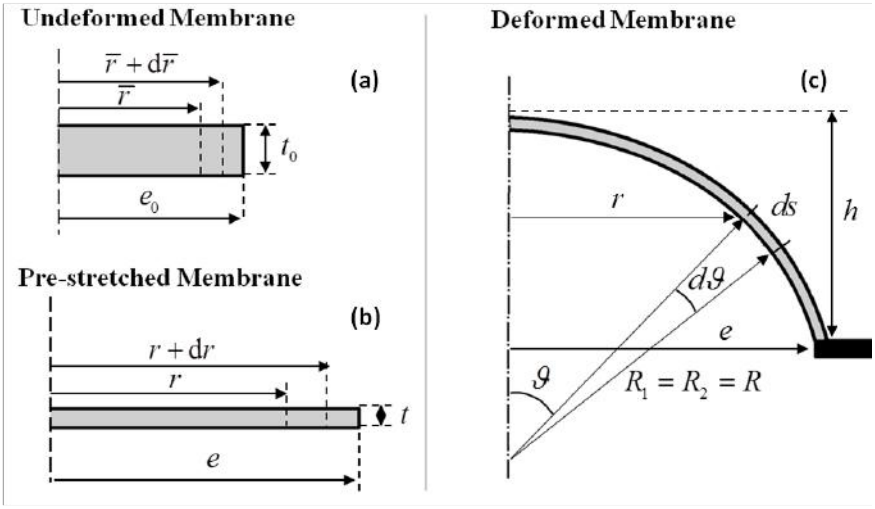

FIGURE 2-1. CIRCULAR DIAPHRAGM DIELECTRIC ELASTOMER GENERATOR (CD-DEG): (A) CD-DEG UNDEFORMED STATE, (B) CD-DEG PRE-STRETCHED STATE WITH NO DIFFERENTIAL PRESSURE AND ELECTRIC POTENTIAL, (C) CD-DEG DEFORMED STATE WITH DIFFERENTIAL PRESSURE AND/OR ELECTRIC POTENTIAL.

The opposing sides of the CD-DEG are subjected to the time variable differential pressure, either generated by pressurization/depressurization of an air volume beneath the CD-DEG or by displacement of a water volume contacting one of the faces of the CD-DEG. The CD-DEG undergoes an out of plane axi-symmetric (bubble-like) deformation (area expansion). In Figure 2-1(c), *h* identifies the resultant displacement of the CD-DEG tip.

A mathematical model for the CD-DEG is widely described in [2]. The model relies on the assumptions that the CD-DEG deforms as a thin spherical shell segment with tip height *h* and radius *R*, the deformation is equi-biaxial everywhere on the DEG, the CD-DEG capacitance is equivalent to that of a planar capacitor with variable thickness.

With the abovementioned assumptions, the principal stretches (circumferential and meridian) of an element of membrane located at a distance $\bar{r}$ from the axis in the undeformed configuration (Figure 2-1 (a)) read as:

$$\lambda\left(h,\bar{r}\right)=\lambda_1\left(h,\bar{r}\right)=\lambda_2\left(h,\bar{r}\right)=ee_0\left(h^2+e^2\right)\Big/\left(e^2e_0^2+h^2\bar{r}^2\right) \qquad (1)$$

The CD-DEG capacitance in a generic deformed configuration (identified by the tip displacement, *h*) is computed by integration of the infinitesimal capacitance element as follows:

$$C_{DEG}\left(h\right)=\int_0^{\arcsin\left(e/R\right)R}\varepsilon\frac{2\pi n^2 r}{t}\mathrm{d}s=\frac{\pi\varepsilon n^2 ee_0}{3t_0}\lambda_{\mathrm{T}}\left(\lambda_{\mathrm{T}}^2+\frac{e}{e_0}\lambda_{\mathrm{T}}+\frac{e^2}{e_0^2}\right) \qquad (2)$$

where ε is the DE material dielectric constant, *n* is the number of DE/electrode layers in the stack, *r* is the radial distance of the infinitesimal DEG element form the axis, $t=t_0/\lambda^2$ is the local

DEG thickness, d*s* is the meridian length of the infinitesimal membrane element (as shown in Figure 2-1 (c)), *R* is the spherical cap radius, and λ_T is the stretch at the DEG tip, namely

$$\lambda_T(h,\bar{r}=0)=\left(h^2+e^2\right)/\left(ee_0\right). \quad (3)$$

As regards the electric field in a generic location within the CD-DEG, it can be related to the applied voltage, *V*, as follows:

$$E(h,\bar{r})=n\lambda^2(h,\bar{r})V/t_0 \quad (4)$$

2.2 Dielectric Elastomers conductivity

From an electrical point of view, a DEG generator can be represented as a non-ideal variable capacitor (with capacitance C_{DEG}) with a large resistance (R_{DEG}) in parallel (see Figure 2-2). Such in-parallel strain-dependent resistance accounts for dissipative effects due to the leakage current (i_{leak}) flowing through the dielectric layer. If a voltage V_{DEG} is imposed on the DEG, the instant dissipated power due to leakage current is $P_{dis} = V_{DEG}^2/R_{DEG}$, i.e., the dissipated power is inversely proportional to the DEG resistance.

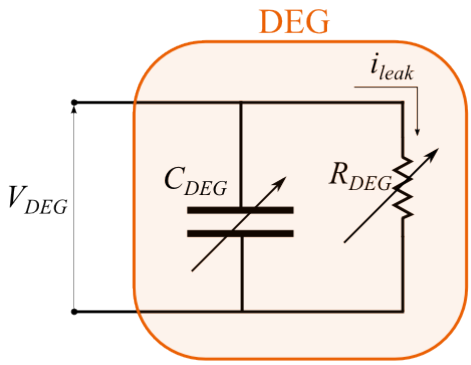

FIGURE 2-2. ELECTRIC SCHEME OF A NON-IDEAL DEG. THE DEG IS REPRESENTED AS A VARIABLE IDEAL CAPACITOR, IN PARALLEL TO A VARIABLE RESISTOR WHICH ACCOUNTS FOR LEAKAGE CURRENT DISSIPATION

For any prescribed DEG layout, R_{DEG} can be estimated by means of the DE material conductivity, κ, which is a material parameter and is independent on the particular DEG geometry and configuration.
In the following, an experimental campaign aimed at measuring the conductivity of a set of DEs is described. DEs conductivity has been measured through a dedicated test bench, suitable to measure other DE features (dielectric constant, break-down field etc.). Measurements have been acquired over a wide range of applied electric field values, with the aim of capturing the dependence of κ on the DE electric loading.

2.2.1 Test and results

Experiments have been conducted using four different commercial DE materials, namely, acrylic VHB-49010 tape, Nusil CF-2186 silicone, Oppo Band natural rubber, and Theraband styrene-based synthetic rubber. For each material, a sample has been prepared pre-stretching a membrane on a rigid frame. The thickness of each sample has been measured after pre-stretching using a laser sensor (Figure 2-3(a)). Electric tests have been performed locating pre-stretched DE samples between cooper compliant electrodes.

Conductivity measurements have been accomplished using a setup similar to that previously employed for the characterization of DE materials dielectric constant and break-down electric field [3]. The setup includes a High Voltage (HV) power supply (10/10B – HS by Trek), controlled through a digital signal generator, which is used to prescribe known voltage on the samples. Current through the DE is measured with a pico-amperometer. Applied voltage is visually checked through an oscilloscope. A picture of the setup is in Figure 2-3(b).

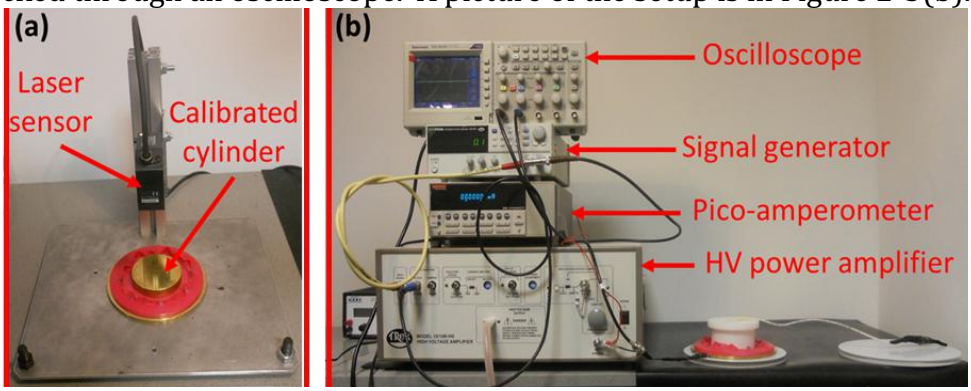

FIGURE 2-3. (A) DE SAMPLE THICKNESS MEASUREMENT THROUGH A LASER SENSOR. (B) APPARATUS FOR LEAKAGE CURRENT MEASUREMENT.

Leakage current is measured through the pico-amperometer by prescribing a constant DC voltage on the DE samples. Each sample has been subjected to increasing voltage values, each of which has been maintained for 20 s. Voltage values have been chosen basing on the measured thickness, in order to produce increasing electric fields on the DE, spaced apart by 10 MV/m. Each measurement (at given voltage, on a specific sample) has been repeated 5 times.
Leakage current measurements allow for an indirect assessment of the DE conductivity, which is simply computed from Ohm's law:

$$\kappa = \frac{i_{leak}}{V_{DEG}} \frac{t}{A} \tag{5}$$

where i_{leak} is the measured current, V_{DEG} is the prescribed voltage, t is the DE layer thickness and A the electrodes area.
Measured conductivity as a function of the applied electric fields for the different DE materials is reported in Figure 2-4. Results show a strong dependence of the conductivity on the applied electric field which, as suggested by [4], can be fit with an exponential relationship in the form $\kappa=\kappa_0\exp(E/E_0)$, where κ_0 and E_0 are constitutive parameters of the material. Fitting curves and the corresponding constitutive parameters are shown in red in Figure 2-4. Measurements results show that VHB has a visibly higher idle conductivity, which surpasses that of the other DEs by almost one order of magnitude.
The exponential trend of conductivity with electric field suggests that, although the cyclic convertible energy of a DEG increases with the square of the applied electric field, the dramatic increase in losses may force to limit operating electric fields, in order to find a compromise between producible energy and dissipation.
A figure of merit for any non-ideal dielectric is the discharging time constant, i.e., a time constant that is proportional to the time of discharge of a capacitor made of the considered dielectric, when it is let free to evolve after an initial charge is placed on its electrodes.

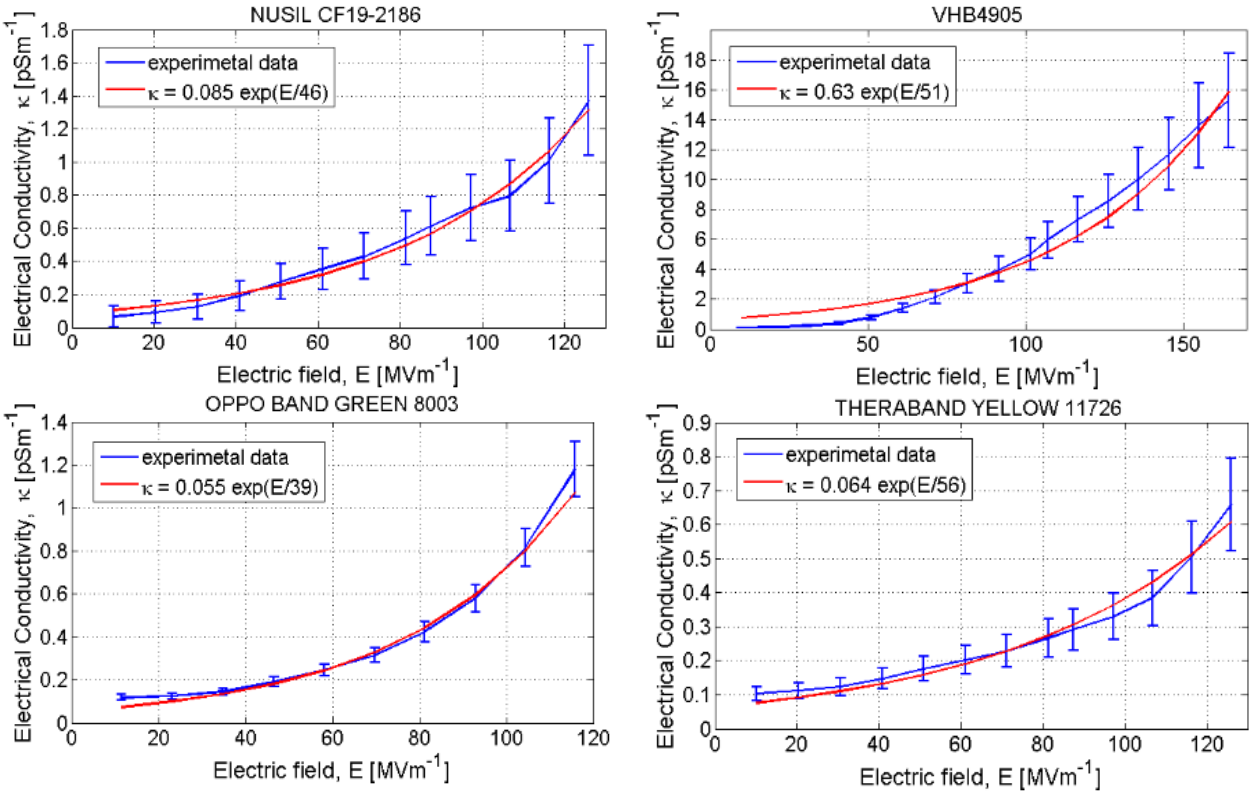

FIGURE 2-4. EXPERIMENTAL RESULTS FOR CONDUCTIVITY MEASUREMENTS AS A FUNCTION OF ELECTRIC FIELD FOR DIFFERENT DE MATERIALS. BLUE LINES WITH ERROR BARS ARE FOR EXPERIMENTAL MEASUREMENTS, WHILE RED LINE ARE FITTING EXPONENTIAL CURVES.

Large conductivity itself might indeed not represent a penalization factor for DEGs, if combined with an exceptionally large dielectric constant. Discharge time constant, on the contrary, provides an order of magnitude of how long should a DEG conversion cycle span in order for the losses to be comparable with the converted energy. Roughly, the influence of leakage currents on DEs performance can be considered negligible if the discharge time constant is much larger than the typical time period of the DEG cycles.
The discharge time constant is a material property that solely depends on the dielectric constant, ε, and conductivity, κ. Considering a plane capacitor of thickness t and surface A, made of the reference dielectric material, the discharging time constant reads as

$$\tau_{DE} = R_{DEG} C_{DEG} = \frac{t}{\kappa A} \frac{\varepsilon A}{t} = \frac{\varepsilon}{\kappa} \qquad (6)$$

Discharging time constant ranges for the reference DE materials are reported in Table 2-1. Due to the dramatic variability of κ with the electric field, uncertainty on the time constant is very large and strongly depends on the applied electric field.

TABLE 2-1. DISCHARGING TIME RANGES FOR THE REFERENCE DES.

DE material	Discharging Time Constant (s)
VHB 4905	3-37
Nusil CF19-2186	18-247
Oppo Band Green 8003	20-241
Theraband Yellow 11726	40-240

It is also worth noticing that all of the considered materials, except for VHB, have a lower-bound time constant which is comparable to typical wave periods, while their time constant dramatically increases (by over one order of magnitude) as the operating electric field is lowered.

2.2.2 Model and projection of results

In this section, we make reference to the CD-DEG architecture to provide an assessment of the leakage losses over a generation cycle as a function of the DE electrical loading.
Non-ideal electric behaviour of a CD-DEG can be modelled through the general scheme depicted in Figure 2-2. In particular, C_{DEG} can be calculated as previously shown in equation (2), while R_{DEG} can be calculated as follows:

$$\frac{1}{R_{DEG}(h)} = \int_0^{\arcsin(e/R)R} \kappa n^2 \frac{2\pi r}{t} \mathrm{d}s \tag{7}$$

Although κ varies through the DEG, as it depends on the electric field E (which varies according to equation (4)), an average value of κ can be used, which is computed at an intermediate value of electric field (between the maximum electric field, at the DEG tip, and the minimum electric field, at the DEG perimeter). With this assumption, the DEG equivalent leakage resistance takes the following close-form:

$$R_{DEG}(h) = \frac{3t_0}{\pi \bar{\kappa}(h) n^2 e e_0 \lambda_T} \left(\lambda_T^2 + \frac{e}{e_0}\lambda_T + \frac{e^2}{e_0^2} \right)^{-1} \tag{8}$$

where $\bar{\kappa}(h)$ can be computed, for example, as the volumetric mean of κ on the CD-DEG:

$$\bar{\kappa}(h) = \frac{2}{e_0^2} \int_0^{e_0} \kappa(h, \bar{r}) \bar{r} \mathrm{d}\bar{r} \tag{9}$$

In the following, we present a case study, using an existing reference DE material and a DEG layout previously sized for an OWC PTO application. The reference DEG layout detailed in Table 2-2 is used for the case study. This layout has been presented in Deliverable 2.3 (D2.3) and it represents a DEG module (out of four total modules) constituting a hypothetic DE PTO for the Spar-OWC WEC. The considered material is Theraband rubber, which, basing on previous results and the analysis above, is among the most promising available materials. It has been previously shown [3] that the break-down field for this material increases with the stretch, following the law in Table 2-2.

We consider a prescribed sinusoidal displacement of the membrane tip, h, with a period T=10 s (i.e., comparable with the period of typical ocean waves), and we analyse a single Energy Harvesting Cycle (EHC). In accordance with established control strategies, we assume that there are two EHCs per wave period (one associated with upward DEG deformation, and one for downward displacements), and, in each cycle, the DEG is electrically active only while its capacitance decreases, i.e., for a time $T/4$ in each cycle.

TABLE 2-2. DEG LAYOUT FOR THE CASE STUDY ON LEAKAGE CURRENT LOSSES

Parameter	Simulation 1
DE material	Theraband Yellow 11726
Dielectric constant [3], ε	2.7×8.85e-12 F/m
Break-down electric field [3], $E_{BD} = E_{BD,0}\lambda^R$	$E_{BD,0}$=97.27 MV/m R=1.022
DEG radius, e	3 m
DEG pre-stretched thickness, t	99.2 mm
Pre-stretch, λ_p	1.1
Foreseen nr. of layers, n	200 layers

During an EHC, the DEG reaches maximum capacitance which depends on the amplitude of its deformation; it is then activated with an electric field (at the membrane tip) which is a prescribed share of the maximum allowed (break-down) field; while the DEG moves towards the flat configuration, electric field at the tip is kept at a fixed prescribed share with respect to the break-down value. The DEG is then completely discharged (and remaining stored energy is recovered) as it reaches the flat position (minimum capacitance).
Typical energy harvesting cycles are represented in Figure 2-5 on a Charge Voltage, Q-V plane, at three different levels of electric loading, assuming that the oscillation amplitude of the DEG tip is $|h|=e$.

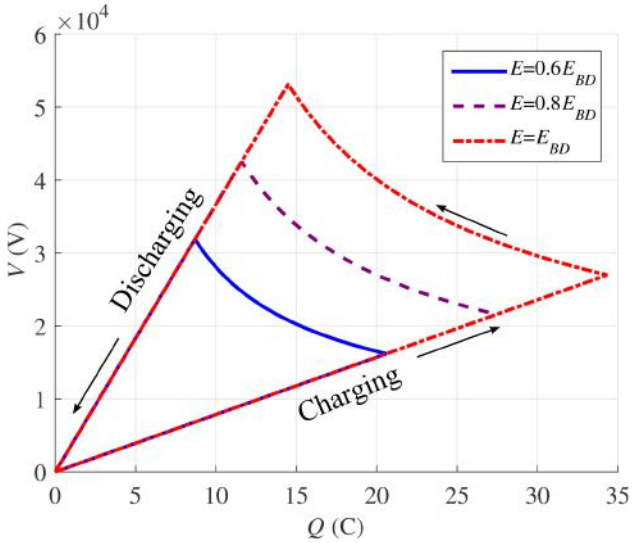

FIGURE 2-5. EHC FOR THE REFERENCE DEG AT DIFFERENT ELECTRIC LOADING LEVELS, IN CORRESPONDENCE OF A DEFORMATION OF THE DEG FROM H=E TO H=0.

We consider a set of DEG oscillations, with period T and with different oscillation amplitudes, from $|h|=0.1e$ to $|h|=e$. For each oscillation, we compute:

- The electric energy generated in a cycle:

$$E_{gen} = -\int V dQ \tag{10}$$

- The electric energy dissipated in a cycle due to leakage currents:

$$E_{diss} = \int_{T/4} \frac{V^2}{R_{DEG}} dt \tag{11}$$

- The average net generated power:

$$P_{net} = \frac{2\left(E_{gen} - E_{diss}\right)}{T} \tag{12}$$

- An efficiency parameter, defined as

$$\eta = \frac{E_{gen} - E_{diss}}{E_{gen}} \tag{13}$$

Results are shown in Figure 2-6. In particular,

- Figure 2-6(a) reports the net power output as a function of the DEG oscillation amplitude, at different levels of applied electric field. Results show that, for the present case, the maximum power output is obtained when the largest electric field is employed, provided that oscillations are rather wide. For small oscillations, on the contrary, dissipations overcome generation, making the use of large electric field inappropriate for energy generation.
- Figure 2-6(b) shows the efficiency as a function of the oscillation amplitude and applied electric field. Although at large deformations the efficiency is quite high, it dramatically decreases and falls to zero as oscillations become small.

Analysis of Figure 2-6(a) and (b) shows that, although efficiency increases by lowering the applied electric field, the net amount of generated energy, at large deformations, is monotonically increasing with the applied electric field.
These results suggest that, with state-of-art materials, the CD-DEG can work efficiently only above a threshold of deformation. I.e., in a real-sea operation perspective, in presence of irregular waves and variable sea conditions, the DEG should be better activated only in those cycles where deformation is sufficient, while it should be left idle when its deformation is lower than approx. $0.3e$. A partial energy recovery in presence of small waves is still possible, but this requires the employment of optimized electric activation, lower than that employed in nominal conditions.

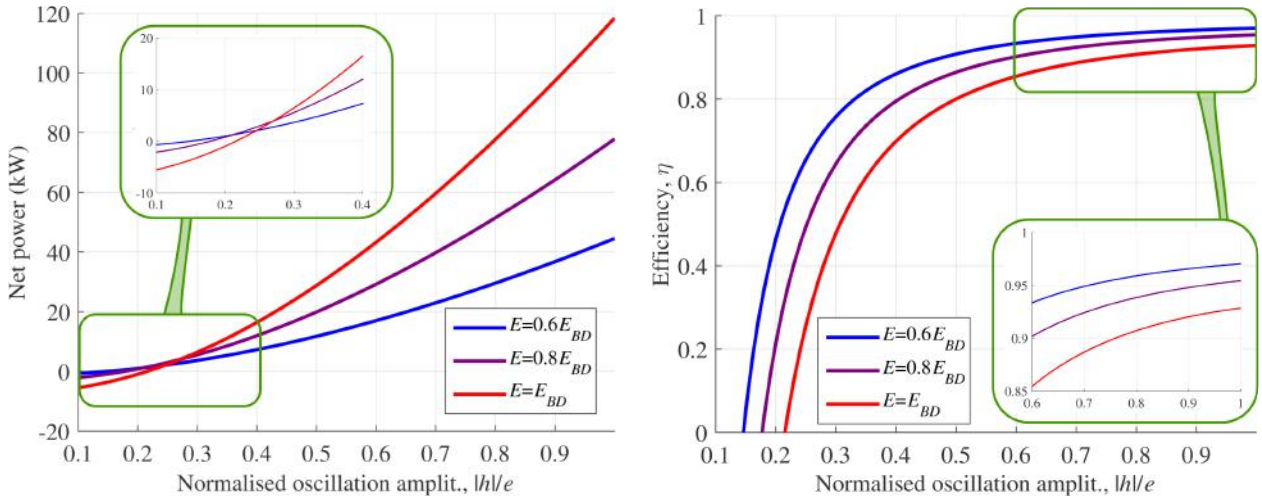

(a) (b)

FIGURE 2-6. (A) NET POWER GENERATED BY THE DEG, INCLUDING LEAKAGE DISSIPATIONS, IN THE HYPOTHESIS OF A 10 S PERIOD WAVE, TIP OSCILLATIONS AMPLITUDES WITH INCREASING AMPLITUDE AND DIFFERENT ELECTRIC LOADING PARTIALIZATION. (B)EFFICIENCY AS A FUNCTION OF THE DEG OSCILLATION AMPLITUDE AT DIFFERENT LOADING LEVELS.

In general, the presented results show that, with available DE materials, the influence of leakage currents on the DEG performance is non-negligible. However, commercial materials are not conceived for DE applications, and it is expected that DE performance could be significantly improved through the employment of optimized materials, specifically thought for energy harvesting applications.

Looking forward to the commercialization of new optimized DE materials, that are expected to be purposely developed for DEG applications in a few years [5], it is expected that DEs conductivity could be decreased by roughly one order of magnitude. To this extent, we re-compute the results obtained in Figure 2-6(b), assuming that the DE material conductivity is 10 times lower (but still presents exponential dependence on the electric field). Updated results are in Figure 2-7, and they show that, with improved conductivity, positive generation is possible even at very small deformations (still with reduced efficiency), while at large deformations efficiency is far larger than 90%.

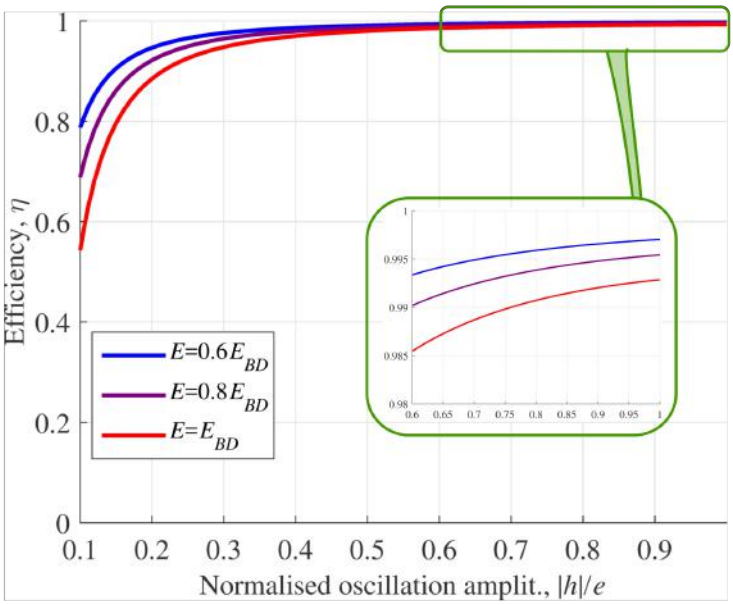

FIGURE 2-7. PROJECTION OF DEG EFFICIENCY AS A FUNCTION OF DEG DEFORMATION AMPLITUDE AND ELECTRIC FIELD, IN THE HYPOTHESIS THAT CONDUCTIVITY IS IMPROVED BY A FACTOR 10.

2.3 Electrodes resistivity

In this section, the focus is set on the analysis of electric losses due to non-infinite conductivity of stretchable electrodes. Deformable electrodes for DEGs are a crucial component, as they must combine high conductivity and large deformations. Research effort is being spent on this topic [6], and viable solutions for large-scale deformable electrodes appear to be thin metallic films (which, however, feature reduced extensibility and higher cost) or conductive polymeric layers, obtained by dispersing conductive particles within a polymeric substrate.

In a first approximation, electrodes resistance is in-series to the DEG capacitance. The low currents produced by the DEG due to its deformation, combined with the intrinsically low value of electrodes resistivity, make dissipation on the electrodes far lower (negligible) with respect to leakage losses during most of the EHC. However, electrodes resistivity may play a crucial role during the DEG charging/discharging phases, i.e., at the beginning and at the end of each EHC, when very large currents are likely to arise. During these short transients, indeed, dissipation on the electrodes is far larger than that due to leakage currents (which contribute to the R-C DEG dynamics as a resistor in-parallel to the DEG capacitance). Electrodes resistivity has to be taken into account to set an upper-bound of applied current during DEG charging/discharging. As a limit-case example, if a voltage step was applied on the DEG to charge it, an infinite current would arise at time t=0 (i.e., in correspondence of the voltage jump) that would be responsible for 50% of the supplied energy to be stored in the capacitor and the other 50% to be dissipated (regardless resistance values in the circuit).

In the following, experimental measurements on resistivity of conductive electrodes spread on a DE substrate are presented. A mathematical model to assess the voltage distribution and energy dissipation during CD-DEG charging/discharging phase is then drawn. The model shows that, with current electrodes resistivity, low energy dissipations can be achieved even in presence of reasonably high currents, which allow for fast charging/discharging of the DEG.

2.3.1 Test and results

Tests have been carried out to measure the sheet resistance of compliant electrodes. For a thin film, sheet resistance R_s is defined as the ratio between resistivity and film thickness, it has the dimensions of a resistance and it is measured in Ω/□ [7]. Sheet resistance is a measure of surface resistance of an electrode. Since charge conduction on the electrode can be considered a surface phenomenon, it is expected that sheet resistance is invariant under scaling of the film contact, and remains the same at different size scales.

Two types of deformable electrodes have been characterized: 1) Thin film golden electrodes on a natural rubber DE (Oppo Band Green) substrate, obtained by metal sputtering on the DE; 2) Polymeric sheet electrodes obtained by dispersion of carbon particles within a silicone matrix and spreading the resulting mix on a chemically affine DE substrate (Elastosil by Wacker) to guarantee bonding. Samples were prepared according to the procedure described in [9]. Pictures of the experimental specimens are in Figure 2-8(a) and (b) respectively.
Sheet resistance is measured positioning an insulating plaque on the specimens, which holds a high-conductivity material at the two edges (whose resistance is far lower than the measured one), and measuring the resistance between the plaque edges with a multimeter (see Figure 2-8(c)). To prevent edge effects, the width, w, of the plaque is much larger than its length (d). Sheet resistance is easily obtained from measured resistance, R_M, knowing the plaque length (d) and width (w): $R_s = R_M \, w/d$.

The following values have been obtained:

- Rs=17 Ω/□ for Au electrodes
- Rs=345 Ω/□ for silicone electrodes

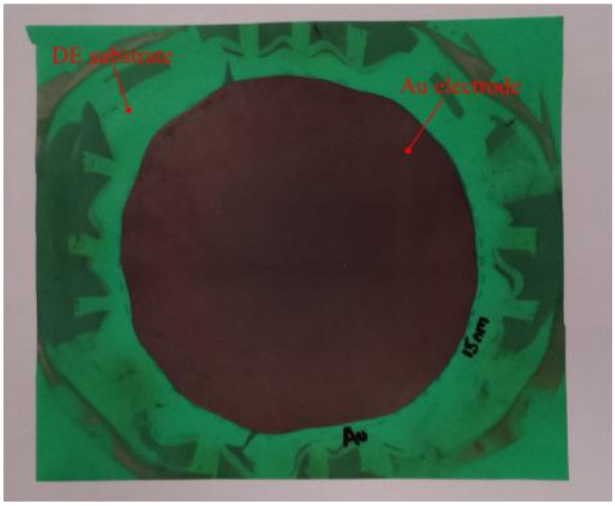

(a)

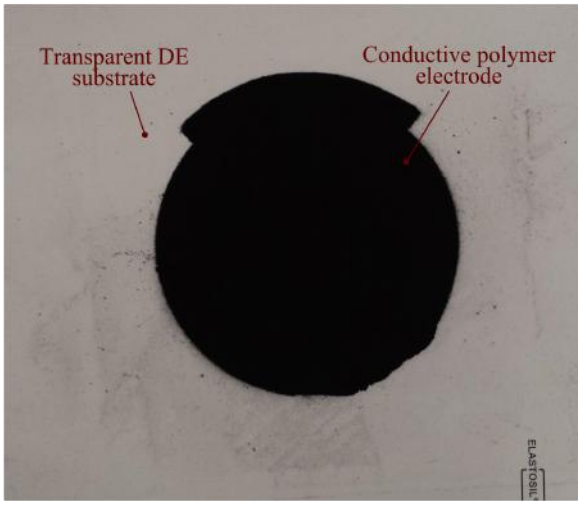

(b)

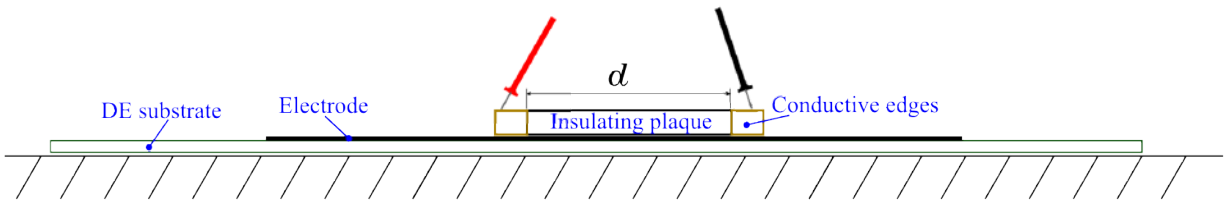

(c)

FIGURE 2-8. (A) GOLDEN ELECTRODE ON A NATURAL RUBBER DE SUBSTRATE; (B) CONDUCTIVE SILICONE ELECTRODE ON A SILICONE DE SUBSTRATE. (C) SETUP FOR SHEET RESISTANCE MEASUREMENT.

The following values have been obtained:

- Rs=17 Ω/□ for Au electrodes
- Rs=345 Ω/□ for silicone electrodes

As expected, Au thin film has much lower resistance. However, due to its lower cost, higher resistance to large stretch, and ease of manufacturing, silicone electrodes appear a much more reasonable solution for industrial applications.

2.3.2 Model and projection of results

In this subsection, a mathematical model for CD-DEG charging/discharging is presented. An analytic solution for the voltage distribution over the electrode is presented for the case with flat DEG (i.e., during discharge), while for the case with inflated CD-DEG (during charging), governing equations are solved numerically. The model allows to set a threshold to the maximum current applied on the DEG to limit Joule effect losses.
We refer to a single layer of a generic CD-DEG, whose deformation is identified by tip elevation h (see Figure 2-9(a)). The following assumptions are done:

- The kinematics of deformation is described by the abovementioned CD-DEG lumped-parameter model.

- The problem is axi-symmetric. This assumption holds only if applied voltage/currents are homogeneous along the DEG perimeter. In practice, this can be enabled by providing the CD-DEG electrodes perimeter with highly conductive layers.

- As the layer is thin, opposite electrodes can be assumed to have the same curvature. Due to symmetry, the mean surface in between the layer faces is equipotential. For simplicity, we set potential V=0 on the layer mean surface, so that a steady-state voltage difference of V is split as $\pm V/2$ on opposite electrodes. Generally speaking, the charge/voltage distribution in opposite electrodes can be considered symmetric.

- We assume that the voltage gradient in circumferential and meridian direction is much lower than the gradient through the membrane thickness. Therefore, we assume that resulting electric field is perpendicular to the DEG electrodes and, even during transients, infinitesimal circumferential DEG rings (as depicted in Figure 2-9(a)) can be treated as parallel-plate capacitors in parallel.

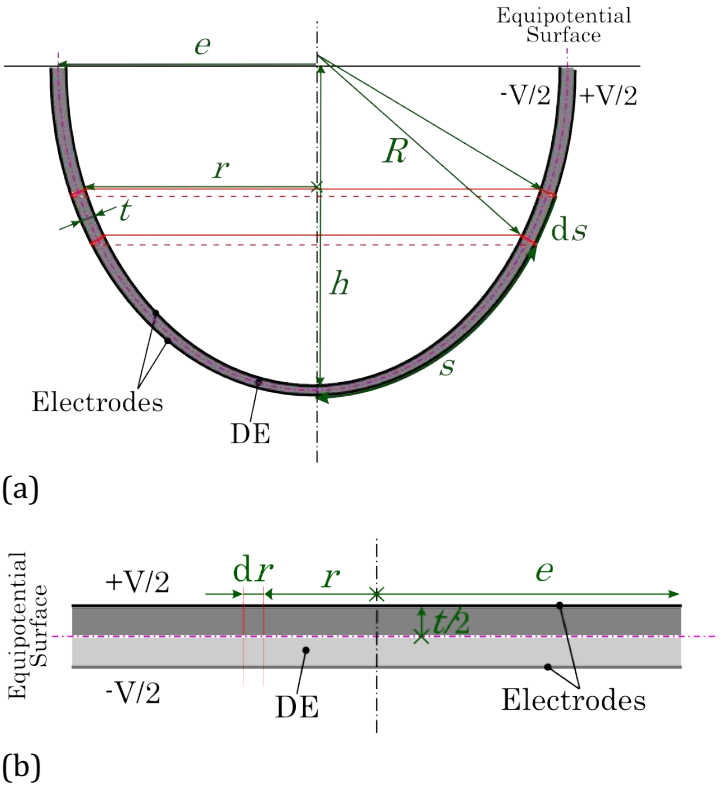

FIGURE 2-9. (A) CD-DEG IN THE INFLATED CONFIGURATION. THE INFINITESIMAL RING ELEMENT IS TREATED AS A PARALLEL-PLATE CAPACITOR. MEAN SURFACE BETWEEN THE FACES IS EQUIPOTENTIAL DUE TO SYMMETRY. (B) CD-DEG IN THE FLAT CONFIGURATION.

The problem is axi-symmetric and it can be described by two variables: time, *t*, and a spatial coordinate. We define generalised coordinate *s* as the meridian distance of a generic point on the DEG from the tip (Figure 2-9(a)). Moreover, we indicate with $r(s)$ the distance of a generic DEG ring from the DEG axis. Finally we call $q(s,t)$ the amount of charge that, at time *t*, lies within the positive electrode portion identified by *s*. The corresponding current through the perimeter of such electrode cap is given by

$$i(s,t)=\frac{\partial q(s,t)}{\partial t} \tag{14}$$

We then define the voltage on the parallel lines identified by coordinate *s* at time t as $v(s,t)$. Considering an infinitesimal electrode ring element (Figure 2-9(a)), Ohm's law yields to:

$$v(s+ds,t)-v(s,t)=dR\cdot i(s,t), \quad \text{with} \quad dR=\frac{ds}{2\pi r(s)t_e(s)\kappa_e} \tag{15}$$

where κ_e is the electrode conductivity, and $t_e(s)$ is its thickness (in general, dependent on the local stretch). Equation (15), combined with (14), takes the following form:

$$\frac{\partial v(s,t)}{\partial s}=\frac{1}{2\pi r(s)t_e(s)\kappa_e}\frac{\partial q(s,t)}{\partial t},\quad \text{i.e.,}\quad \frac{\partial v(s,t)}{\partial s}=\frac{R_s}{2\pi r(s)}\frac{\partial q(s,t)}{\partial t} \tag{16}$$

where the sheet resistance, R_s, definition has been introduced.
As each DEG infinitesimal ring is treated as a parallel-plate capacitor, the following relation holds:

$$q(s+ds,t)-q(s,t)=dC\cdot v(s,t),\quad \text{with}\quad dC=\frac{4\pi\varepsilon r(s)\,ds}{t_l(s)} \tag{17}$$

where $t_l(s)$ is the DE layer thickness. Equation (17) leads to:

$$v(s,t)=\frac{t_l(s)}{4\pi\varepsilon r(s)}\frac{\partial q(s,t)}{\partial s} \tag{18}$$

Upon recombination of equations (16) and (18), the following Partial Differential Equation (PDE) for $v(s,t)$ is obtained:

$$\frac{\partial v(s,t)}{\partial t}=\frac{t_l(s)}{2\varepsilon r(s)}\frac{\partial}{\partial s}\left(\kappa_e t_e(s) r(s)\frac{\partial v(s,t)}{\partial s}\right) \tag{19a}$$

$$\text{or}\quad \frac{\partial v(s,t)}{\partial t}=\frac{t_l(s)}{2\varepsilon r(s)}\frac{\partial}{\partial s}\left(\frac{r(s)}{R_s}\frac{\partial v(s,t)}{\partial s}\right) \tag{19b}$$

This equation has to be combined with a set of initial and boundary conditions, and its solution provides the time history of the voltage on the DEG electrodes.
Initial condition is $v(s,0)=0$ if the DEG has initially no charge, or $v(s,0)=V/2$ if a voltage difference V is initially applied to the DEG electrodes.
As regards boundary condition, one condition provides the prescribed voltage or current at the layer perimeter, i.e., at $s=\arcsin(e/R)R$ (provided that the DEG is a spherical cap). Owing to axi-symmetry, the other condition reads as:

$$\frac{\partial v(0,t)}{\partial s}=0. \tag{20}$$

In the following, the presented problem is solved in the following for two cases: discharge of the flat DEG (at the end of the EHC); charge of the inflated DEG (with reference to the emispheric deformed configuration).

<u>Flat DEG discharging</u>
According to the mentioned control strategy, the DEG is discharged at the end of each EHC, as it reaches the flat configuration.

In this particular case, the DE layer configuration is shown in Figure 2-9(b): coordinate *s* coincides with *r*, and the electrode thickness is homogeneous.
Indicating with *V* the voltage initially applied on the DEG and with $C_{DEG,f}$ the capacitance in the flat position, we assume that a constant discharging current *I* is homogeneously picked up through the layer perimeter for a time $\tau = C_{DEG,f} V / I$, so that the DEG is fully discharged. Successively, the current at the DEG perimeter is set to zero, and the voltage on the electrodes becomes homogeneously null. The time τ is hereafter referred to as "active discharging/charging time", as opposed to the total characteristic time expressing the duration of the transient charging/discharging phases.
With this assumption, the PDE problem reads as follows:

$$\begin{cases} \dfrac{\partial v}{\partial t} = \alpha \dfrac{1}{r} \dfrac{\partial}{\partial r}\left(r \dfrac{\partial v}{\partial r} \right), \quad \text{with} \quad \alpha = \dfrac{\kappa_e t_e t_l}{2\varepsilon} \\ v(r,0) = V/2 \\ \dfrac{\partial v(0,t)}{\partial r} = 0 \\ \dfrac{\partial v(e,t)}{\partial r} = -\dfrac{I}{2\pi e \sigma_e t_e} \Pi\left(\dfrac{t-\tau}{2} \right) \end{cases} \tag{21}$$

where $\Pi(x)$ is the rectangle function.
Differential problem (21) is in a well-known mathematical form most often referred to as "heat equation" in cylindrical coordinates, as it describes many diffusion phenomena as heat transfer or mass transport in a porous medium. A number of analytical methods exist to tackle this problem, e.g., using Green's functions and variables separation [8]. The analytic solution is as follows:

$$v(r,t) - \frac{V}{2} = \varphi(r,t) = \begin{cases} -\dfrac{I}{\pi \kappa_e t_e e^2} \left[\alpha t + \sum_{n=1}^{\infty} \dfrac{\mathrm{J}_0(\beta_n r)}{\mathrm{J}_0(\beta_n e)} \dfrac{1 - \exp(-\alpha \beta_n^2 t)}{\beta_n^2} \right], & \text{if} \quad 0 \le t < \tau \\ \dfrac{2}{e^2} \left[\Im_0 + \sum_{n=1}^{\infty} \dfrac{\mathrm{J}_0(\beta_n r)}{\mathrm{J}_0^{\,2}(\beta_n e)} \Im_n \exp\left(-\alpha \beta_n^2 (t-\tau)\right) \right], & \text{if} \quad t > \tau \end{cases} \tag{22}$$

where J_0 is Bessel function of first kind and order zero, β_n is a sequence of non-null eigenvalues satisfying the following equation:

$$J_1(\beta_n e) = 0, \tag{23}$$

and $\Im_n$ are defined as follows:

$$\Im_0 = \int_0^e r' \varphi(r', \tau) dr', \quad \Im_n = \int_0^e r' \mathrm{J}_0(\beta_n r') \varphi(r', \tau) dr' \quad \text{for} \quad n = 1, 2, \tag{24}$$

The energy recovered from the DEG through its discharge can be computed upon integration over time of the power flowing through the DEG perimeter, $P_{out}(t)=2nv(e,t)I$, where n is the number of layers and the factor 2 owes to the abovementioned choice of the zero of the potential. As I is set to zero after a time τ, energy is extracted from the DEG only until $t<\tau$.
We take as reference the CD-DEG described in Table 2-2, and we use equation (22) to display the voltage distribution on the positive electrode and its variation with time. For the calculation, we assume that the electrode has shear resistivity $R_s=1/(\kappa_e t_e)=345$ Ω/□ (as previously measured on the conductive silicone specimen). The initial voltage on the DEG layers is V=53 kV (corresponding to the maximum discharge voltage in Figure 2-5).
The voltage distributions on the DEG electrodes at different instants (spaced apart by 1 μs) are shown in Figure 2-10, where a discharging current of 150 A on each layer has been assumed. This extremely high current is far above plausible currents that will be employed in practice, and it would provide discharge of the DEG in an extremely short time, such as τ≈0.5 ms. This value has been however used in this example to emphasize the non-homogeneity of voltage distribution on the electrode.

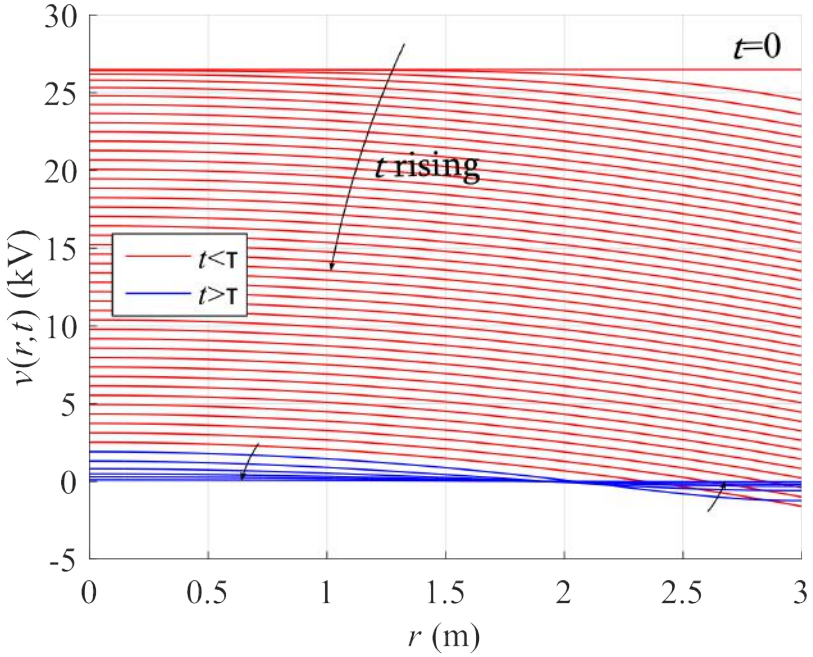

FIGURE 2-10. DISTRIBUTION OF VOLTAGE ON THE DEG ELECTRODES AT DIFFERENT TIME INSTANTS. RED LINES REFER TO THE FIRST PHASE OF THE TRANSIENT, WHEN A CONSTANT CURRENT *I* IS GATHERED AT THE ELECTRODES PERIMETER. BLUE LINES REFER TO THE FINAL TRANSIENT, WHEN CURRENT ON THE LAYERS BORDER IS SET TO ZERO.

Figure 2-10 shows that DEG discharging takes place according to the following mechanism:

- As a constant current is gathered through the electrodes perimeter, voltage on the DE layers progressively decreases. However, due to electrodes resistivity, voltage at the layers perimeter is lower than the voltage in the centre (see red lines in Figure 2-10).
- After a time τ, current is interrupted, as the net amount of removed charge equals the total initial charge on the electrode. Nonetheless, voltage on the electrode is not homogeneously-null, and it results negative (reverted polarity) at the perimeter and positive at the centre.

- During the successive phase, the DEG evolves freely in absence of external current, opposite charges on the electrodes redistribute and voltage progressively flattens to a null value.

In the present example, the discharging transient (from t=0 to the instant where the voltage is homogeneously null) has a duration of approximately 1.1τ.
The example demonstrates that, if the applied current is very high (or, reversely, if the electrodes resistivity is too large), inhomogeneity in voltage distribution can arise, which is responsible for energy dissipation, DE layers heating by Joule effect, and longer transients for voltage stabilization.

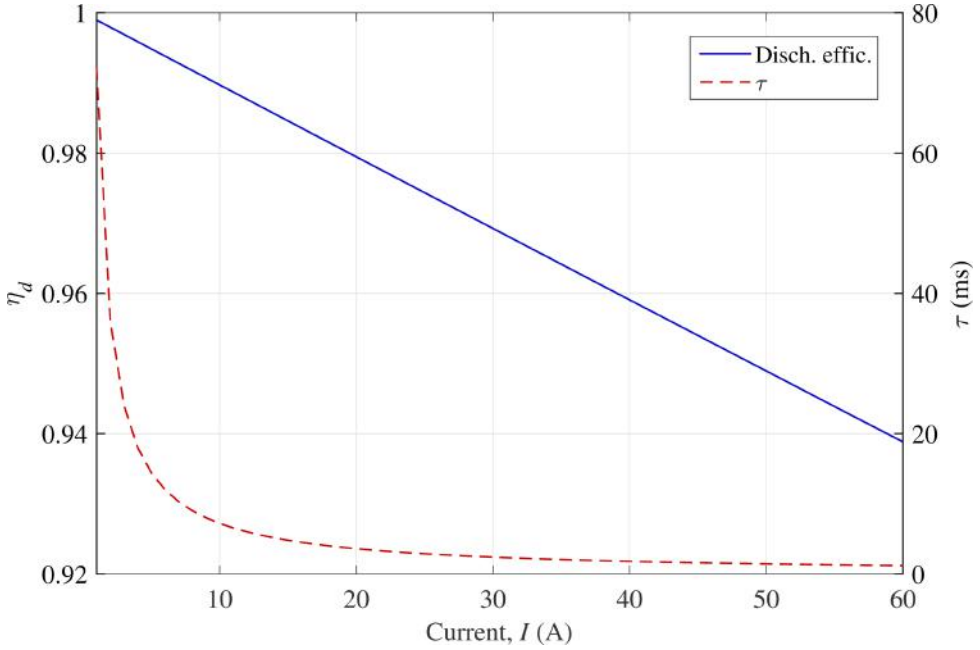

FIGURE 2-11. DEG DISCHARGING EFFICIENCY AND ACTIVE DISCHARGING TIME AS A FUNCTION OF THE IMPOSED CURRENT ON EACH LAYER.

With reference to the presented case study, Figure 2-11 reports the DEG discharge efficiency, η_d (defined as the ratio between the energy positively collected through the electrodes perimeter and the initial electrostatic energy in the DE layers) and the corresponding active discharging time, τ, as a function of the discharging current I applied on each layer. As expected, the discharging efficiency decreases with increasing current, as the transient becomes faster. Nevertheless, results show that, with the current values of compliant electrodes conductivity, extremely high efficiencies are reached, draining each layer with currents in the order of a few Amperes, which still guarantee very short discharging time.

Inflated DEG discharging

DEG charging can be investigated using the general form of equation (19) and solving it through numeric techniques. Charging transients and the corresponding efficiencies are studied in the most critical case, when the DEG deformation is maximum (e.g, emispherical inflated configuration), i.e., when capacitance is maximum and electrodes thickness is minimum.
Assuming that the DEG is charged through a constant current I, the following PDE in $v(r,t)$ applies:

$$\begin{cases} \dfrac{\partial v(s,t)}{\partial t} = \dfrac{t_l(s)}{2\varepsilon r(s)} \dfrac{\partial}{\partial s}\left(\kappa_e t_e(s) r(s) \dfrac{\partial v(s,t)}{\partial s} \right) \\ v(s,0) = 0 \\ \dfrac{\partial v(0,t)}{\partial s} = 0 \\ \dfrac{\partial v(\pi e/2,t)}{\partial s} = \dfrac{I}{2\pi\kappa_e t_e e} \Pi\left(\dfrac{t-\tau}{2} \right) \end{cases} \quad (25)$$

where the active charging time, τ, depends on the charging voltage and on the inflated DEG capacitance: $\tau = C_{DEG,i} V / I$.

The problem can be solved with a PDE solver. We used the PDE mode in Comsol multi-physics 3.5.

Two limit cases are considered: in a first scenario, the sheet resistance of the electrodes is considered constant throughout the electrode and equal to that in the flat case (R_s=345 Ω/□); in the second scenario, the conductivity is assumed constant and equal to that in the flat configuration (κ_e=58 S/m) and the electrode thickness is assumed to vary with stretch in the same fashion of DE layers.

As in the previous example, voltage distributions relative to a very high charging current (150 A) are shown to emphasize the effect of voltage resistivity. Basing on the full-load cycle in Figure 2-5, the charging voltage for the reference DEG is taken equal to V=27 kV.

Results for the two considered scenarios are reported in Figure 2-12(a) and (b) respectively.

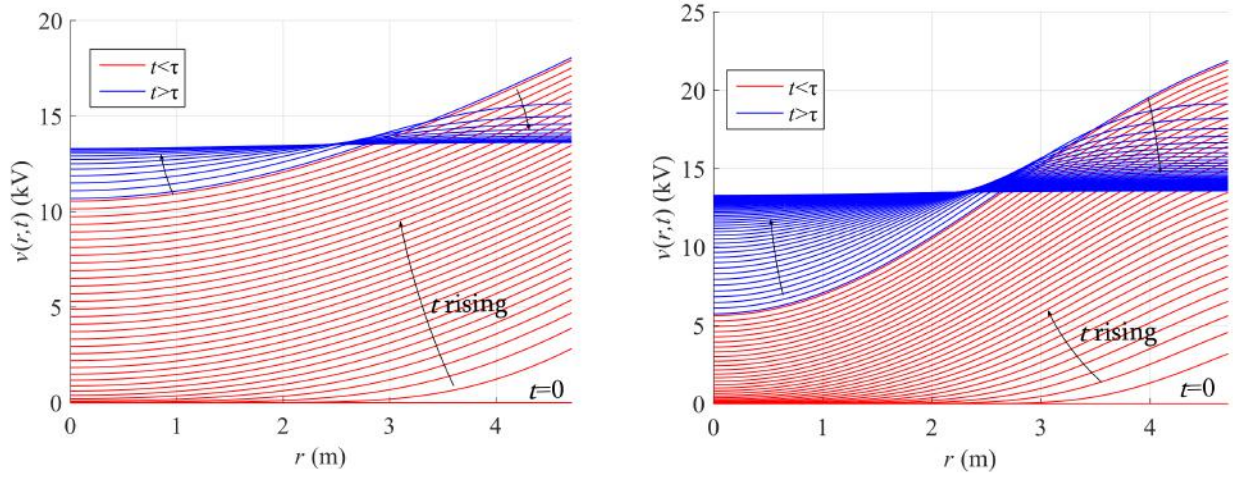

(a) (b)

FIGURE 2-12. DISTRIBUTION OF VOLTAGE ON THE DEG ELECTRODES AT DIFFERENT TIME INSTANTS. RED LINES REFER TO THE INSTANTS DURING WHICH CURRENT IS POSITIVELY SUPPLIED TO THE DEG, WHILE BLUE LINES ARE FOR THE FREE EVOLUTION OF THE SYSTEM IN ABSENCE OF EXTERNAL CURRENT. VOLTAGE PROFILES ARE OBTAINED UNDER DIFFERENT HYPOTHESES: (A) THE ELECTRODE SHEET RESISTANCE IS CONSTANT AND INDEPENDENT ON DEFORMATION. (B) THE ELECTRODE RESISTIVITY IS CONSTANT, WHILE THE ELECTRODE THICKNESS VARIES WITH $1/\Lambda^2$.

The plots show that, conversely with respect to the discharging case, as current is supplied to the DEG, voltage at the DE edge is larger than in the middle. After a first phase, during which current is supplied, a free evolution phase (with no external current) is necessary to achieve flat voltage distribution on the electrode.
Comparison with discharging results at the same current (Figure 2-10) shows that inhomogeneity in voltage distribution is greater, due to the large capacitance of the DEG in this configuration. Comparison of Figure 2-12(a) and (b) shows that the effect of variable electrode thickness might provoke visibly larger gradients and longer transient times. The active charging time is τ=1.1 ms, and the time after which voltage distribution is flat is approximately 1.7τ for the case of Figure 2-12(a) and 2.3 τ for the case of Figure 2-12(b).

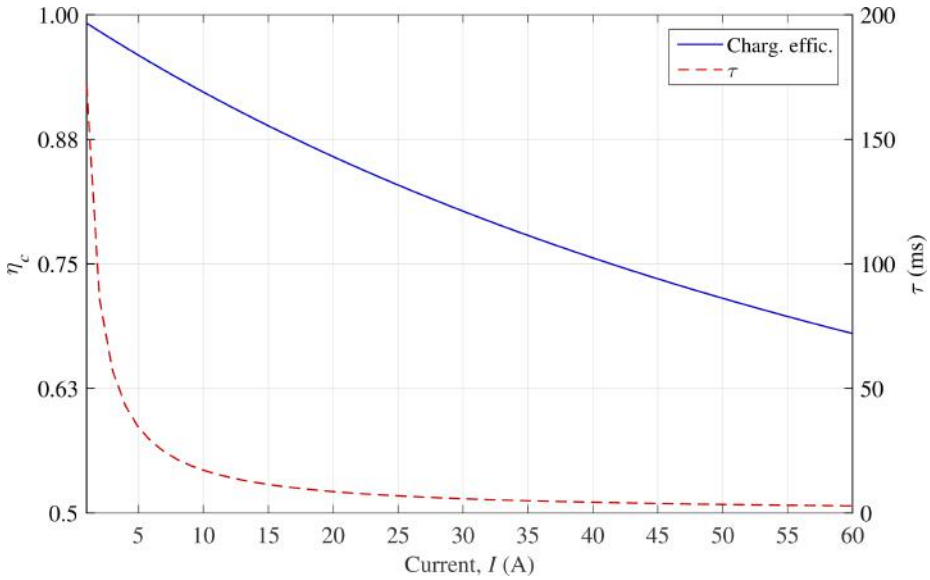

FIGURE 2-13. DEG CHARGING EFFICIENCY AND ACTIVE CHARGING TIME AS A FUNCTION OF THE IMPOSED CURRENT ON EACH LAYER.

For the most conservative case, i.e., assuming that electrodes resistance increases with decreasing thickness, Figure 2-13 reports the DEG charging efficiency, η_c (defined as the ratio between the energy effectively stored in the device and the total energy supplied to the DEG through the electrodes perimeter) and the corresponding active charging time, τ, as a function of the charging current I applied on each layer. The picture shows that, with the pessimistic assumption of electrodes resistivity dramatically increasing with deformation, charging currents in the orders of a few Amps still provide DEG charging in an acceptable time (hundreds of ms) with very high efficiency (well above 90%). The situation would be even improved (lower charging time, higher efficiency) in those cycles where the maximum DEG deformation is $h<e$.

In conclusion, the analysis carried out on energy dissipation due to electrodes resistivity has proven that state-of-art conductive polymer materials are suitable to build large-scale compliant electrodes, which provide high DEG charging/discharging efficiencies and proper timing with respect to characteristic EHC times.

3. STUDY OF DIRECT CONTANT

The suitability dielectric and conductive deformable materials that are commonly employed in DEGS, (acrylic elastomers such as VHB, hydrogels) and system-combinations of these materials for long term application in electroactive membranes of water powered dielectric elastomer generators have been investigated and the respective results are presented and discussed in this section. The experimental investigations involved electrostatic charge decay and breakdown measurements, dielectric impedance spectroscopy and mechanical-to-electrical energy conversion measurements. The experimental techniques are introduced and described at their first appearance together with the discussed materials.

Section 3.1 "Dielectrics" starts with the discussion of results obtained for the acrylic elastomer VHB and the effect of water on the dielectric properties. VHB has been already extensively investigated under dry conditions as a reference material for both small-scale and large-scale dielectric elastomer generators. However, the inter-action between water and VHB has not yet been investigated.

The discussion follows with a focuses on natural rubber as deformable dielectric material and the effect of water on its dielectric properties The material has been investigated in the past for a number of advantageous properties: differently from VHB, natural rubber has very low viscose losses, it is low cost, abundant and can be sustainably sourced. Also the Young's modulus is about one order of magnitude higher than that of VHB, which is advantageous for energy harvesting since it increases the breakdown strength.

Section 3.2 "Electrodes" summarizes the effect of bare water electrodes on VHB and natural rubber. The discussion is continued with a brief note about the influence of water repellent surface treatments by various oils and greases.

The main part of section 3.2 discusses the performance of polyacrylamide hydrogel electrodes. The hydrogel electrodes were bounded to VHB for reference purpose and mechanical-to-electrical energy conversion measurements could be performed.

The final section 3.3 "Encapsulation" discusses the effect of water resistant encapsulation layers made from VHB. The acrylic elastomer VHB was chosen as exemplary materials which can be easily compared to results obtained for non-encapsulated VHB and bare water electrodes.

3.1 Dielectrics

3.1.1 Dielectric testing setup

The investigation and testing of dielectric elastomer materials for their applicability as electroactive membranes for waterbased dielectric elastomer generators were carried out with a custom designed test cell shown in Fig. 3-1. The cell consist of two PMMA cylinder tubes of 40 mm length with an outer and inner diameter of 30 mm and 15 mm respectively. Both tubes are closed at one end with polished stainless steel electrodes. The open sides of the tubes are closed by the sample support rings which are glued to the dielectric sample material under test. The tubes are equipped with filling holes which allow to fill the inner tube volume with tap-water. The tap-water is sufficiently conductive and the sample under test can thus be connected via the electrodes of the system. Characterization measurements were done with VHB elastomers, and natural rubbers.

FIGURE-3-1 EXPLODED VIEW OF TEST CELL FOR WATER BASED MEASUREMENTS OF ELASTOMER MEMBRANES.

VHB elastomer

The acrylic elastomer VHB, produced by the 3M company, has become the quasi standard "work-horse" material for electroactive polymer generators. The VHB elastomer is thus an important reference material for any new development. For applications that require a direct contact of VHB with water no data exist which describe the performance and the suitability of VHB under such conditions. In a series of experimental measurements VHB elastomers of different thicknesses and various stretching ratios were tested in water to characterize the respective charge stability and the overall dielectric stability.

Charge decay

In a first experiment VHB 4910 with a nominal thickness of 1 mm has been tested for its electrostatic charge stability. The charge stability was tested both with compliant electrodes (carbon grease made of ELBESIL B50 siliconoil and carbon black powder from ABCR with an average particle size of 0.42 µm) in air, and without electrodes in water. Measurements in air were done to obtain a reference data set. The arrangement for the reference experiment is schematically outlined in Fig. 3-2.

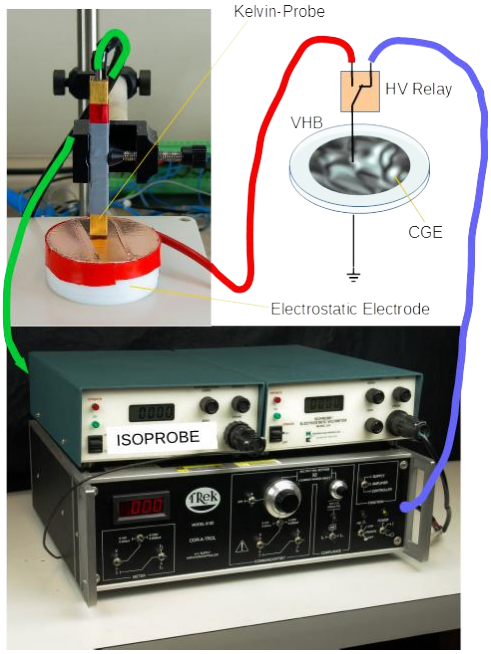

FIGURE-3-2 EXPERIMENTAL ARRANGEMENT OF THE EQUIPMENT FOR CHARGE DECAY MEASUREMENTS. FOR WATERBASED MEASUREMENTS VHB SAMPLES WERE MOUNTED TO THE TEST CELL OF FIG. 3-1.

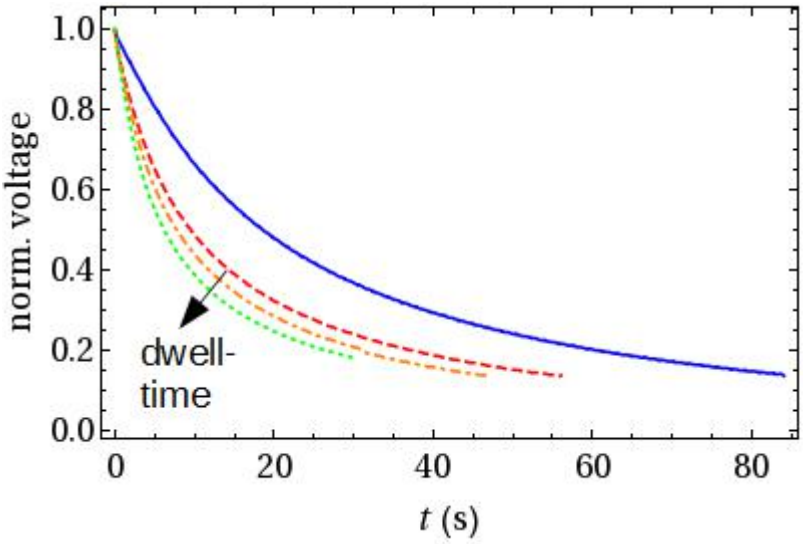

FIGURE-3-3 NORMALIZED VOLTAGE DROP DUE TO CHARGE DECAY OF 1 MM THICK VHB MEMBRANES MEASURED WITH CARBON GREASE ELECTRODES IN AIR (SOLID BLUE), AND IN WATER WITHOUT ELECTRODES (DASHED RED). AN INCREASING DWELL TIME OF THE SAMPLE IN WATER RESULTS IN FASTER CHARGE DECAY CURVES (DOTDASHED ORANGE, AND DOTTED GREEN).

The reference sample with the carbon grease electrodes was first connected to a high voltage source (Trek 610 D) and a dc voltage of >3 kV was applied for some seconds. Right after, the hot electrode was reconnected via a computer controlled high voltage relay to an external, insulated electrostatic electrode where the electrostatic potential could be measured contactless by a Kelvin probe (ISOPROBE Model 244A). As the charges on the carbon grease electrodes decay the electrostatic potential at the insulated electrostatic electrode drops accordingly. At a potential of 3 kV data recording started. The solid blue line in the diagram of

Fig. 3-3 shows the decreasing voltage versus time. The voltage has been normalized to the starting voltage of 3 kV. Approximately 50 % of the charge has decayed after the elapsed time of about t_{50}=20 s. Most small scale harvesting systems work with a cycle period shorter than 5 s. Within 5 s less than 20 % of the collected charge has decayed and energy harvesting is possible with a reasonable efficiency.
The second experiment subjected a new VHB 4910 sample without electrodes to the aqueous environment supplied by the test cell introduced in Fig. 3-1. The electrodes of the test cell were connected to the experimental setup according to the schematic of Fig. 3-2. Right after the test cell had been filled with tap-water a dc voltage of >3 kV was applied for some seconds, followed by a reconnection to the electrostatic electrode and the Kelvin probe. At a potential of 3 kV data recording started. The decay of the normalized potential is plotted in the diagram of Fig. 3-3 as dashed red line. In comparison to the charge decay of the reference sample, the charge decay of the water submerged sample occurs at a much faster rate. Already after 10 seconds more than 50 % of the collected charge has decayed. The decay rate increases even more with progressive dwell-time where the sample remains in contact with water. Successive measurements are plotted in the diagram of Fig. 3-3 as dot-dashed orange, and dotted green lines. Every successive measurement shows an increasing charge decay compared to the preceding measurement. The trace of the last measurement shows that already after 5 seconds almost 45 % of the charge has decayed. The data show qualitatively convincing that the VHB elastomer with direct contact to water cannot be applied in a simple way as an efficient harvesting element.

Impedance spectroscopy

In order to gain better insight into the electrical material properties, and also in order to build a "reference data base" for other materials, the different VHB elastomer were measured and characterized with dielectric impedance spectroscopy. VHB elastomers of different nominal thicknesses, t_n, and with different stretch ratios, λ, were prepared and mounted to the test cell. Impedance measurements were performed within different time intervalls, Δt. The listing below gives an overview over the tested VHB samples:

- sample I t_n=0.5 mm, λ = 1, Δt={0.2 h, 24 h}
- sample II t_n=1 mm, λ = 1, Δt=0 h
- sample III t_n =0.5 mm, λ = 1.87, Δt={ 0.2 h,1 h, 2 h, 4 h}
- sample IV t_n=0.5 mm, λ = 1.87, Δt={0.2 h,1 h, 24 h}
- sample V t_n=0.5 mm, λ = 2.12, Δt={0.2 h, 2 h, 4 h}
- sample VI t_n=0.5 mm, λ = 2.12, Δt={0.2 h, 2 h, 24 h
- sample VII t_n=0.5 mm, λ = 2.12, Δt={0.2 h, 2 h}

The following will present and discuss a selection of important result. The diagrams in Fig. 3-4(a) and (b) shows the real part, Z', and the imaginary part, Z'', of the impedance spectra of sample I and II versus the frequency f. The nominal thicknesses of both samples are 0.5 mm and 1 mm respectively. The solid blue line is the first sample impedance measured right after the

installation to the test cell. The amplitude of of the applied test signal was 500 V. The high voltage amplitude restricted the maximal frequency to 10 kHz. At least up to test amplitudes of 500 V no significant dependence of the impedance on the signal amplitude was found with follow-up measurements. Therefore, all further measurements were done with a signal amplitude of 1 V which allowed an extent of the frequency window up to 20 MHz. The dashed red line is a further measurement of sample I, 24 hours after the installation. During this time the sample was not removed from the test cell and had been in contact with water all time long. The plotted data in the diagram show only subtle changes compared to the first measurement. A slight decrease of the impedance appears in the low frequency regime (<1 Hz), whereas slightly larger and smaller values were measured in the mid-frequency regime (10 Hz < f <10 kHz). The high frequency part shows a relaxation at ca. f=1 MHz. This relaxation is mainly related to the electrical property of the test cell. A further relaxation appears to develop at even higher frequencies.

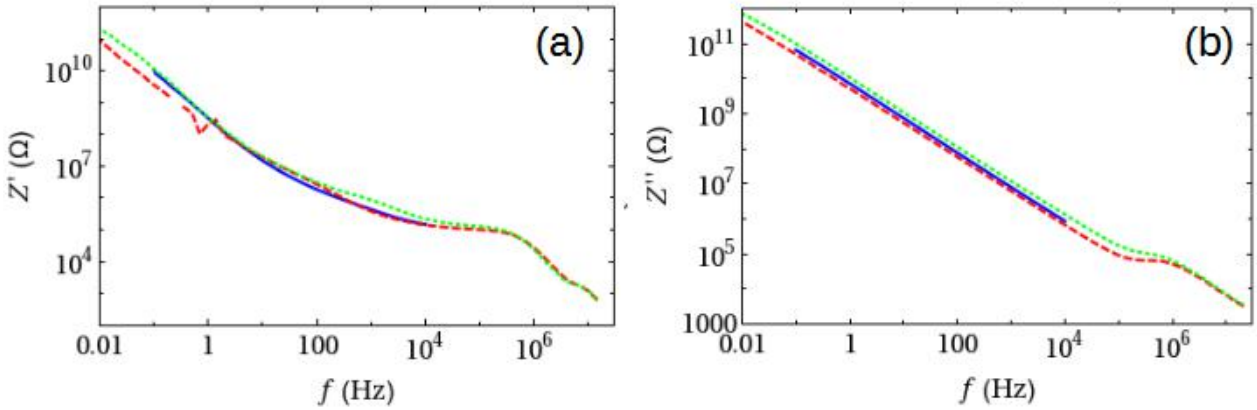

FIGURE-3-4 IMPEDANCE SPECTRA OF VHB MEMBRANES IN WATER. THE DIAGRAMS SHOW THE REAL (A) AND THE IMAGINARY (B) PART OF THE IMPEDANCE. THE IMPEDANCE OF A 0.5 MM THICK VHB (SOLID BLUE) WAS MEASURED WITH A 500 V TEST SIGNAL, AND WITH A 1 V TEST SIGNAL AFTER A 24 H DWELL TIME IN WATER (DASHED RED). THE IMPEDANCE OF A 1 MM THICK VHB (DOTTED GREEN) IS GIVEN FOR COMPARISON.

The kink in the Z' data at frequencies beyond 3 MHz s related to inductive parasitics. The main relaxation, which is related to the dc resistance and the geometric capacitance of the VHB membrane, occurs at frequencies below the experimental frequency window. The impedance at low frequencies of a 0.5 mm thick VHB membrane (dashed red) and the impedance of sample II with the nominal thickness of 1 mm (dotted green) is almost identical. The differences to the impedance of sample I, with just half the thickness, is minute, especially in the important low frequency range. Thus, for reasons of time, all further measurements were performed with samples of 0.5 mm thickness.

Figure 3-5(a) and (b) shows the real and imaginary impedance of the VHB sample IV with a stretch ratio of $\lambda = 1.87$. The data of the first measurement, right after installation, are displayed in the diagrams as solid blue lines. The second measurement is plotted with a dashed red line; it followed 1 hour later after the first measurement. The last measurement happened 24 hours after the first measurement when the sample was brought in contact with water. The impedance data of this last measurement are plotted with dotted green. Markable differences between the impedance data of the three successive measurements appear only within a rather small frequency interval. At frequencies between 1 Hz and 1 kHz the real part, Z', is growing

with increasing dwell time of the sample in water. Also the high frequency relaxation shows a small shift to lower

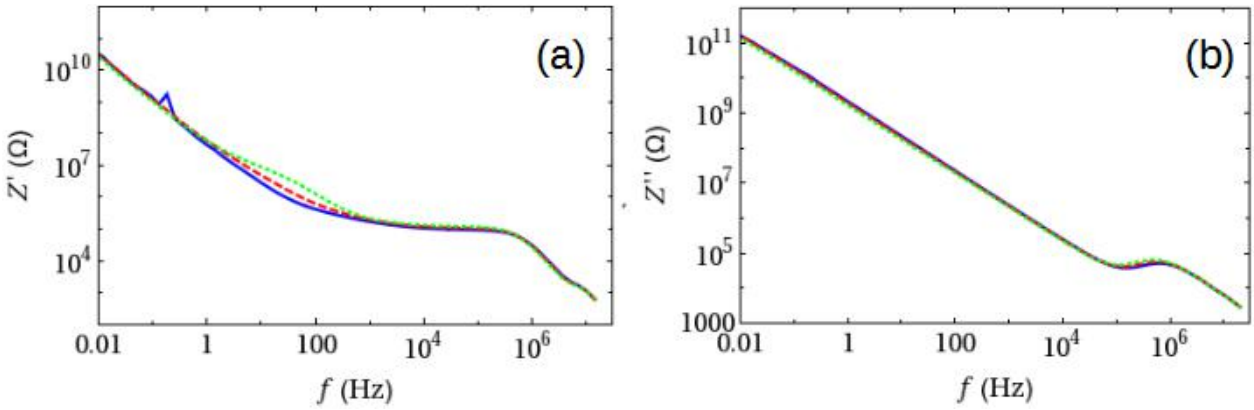

FIGURE-3-5 IMPEDANCE SPECTRA OF A 0.5 MM THICK VHB MEMBRANE, STRETCHED TO A RATIO OF Λ=1.87, IN WATER. THE DIAGRAMS SHOW THE IMPEDANCE SPECTRA RIGHT AFTER INSTALLATION (SOLID BLUE) AND AFTER A DWELL TIME IN WATER OF 1 H (DASHED RED), AND AFTER A DWELL TIME OF 24 H (DOTTED GREEN).

frequencies. In order to understand all these features the data need to be fitted to a model system. Unfortunately, the spectra are not fully defined since the important low frequency relaxations are not expressed but hidden below the lowest test frequency. A fitting procedure will thus not produce a set of reliable material parameters. A reliable data fitting however, turned out to be possible with the impedance data of membranes that have slightly higher stretch ratios.

The general influence of the stretch ratio on the dielectric material properties is displayed with Fig. 3-6. The diagrams in Fig. 3-6(a) and (b) shows the first (Δt=0 h) impedance spectra of the pristine samples I, IV, and VI. The impedance of sample VI, with a stretch ratio of λ =2.12 is plotted with a dotted green line. Only a small difference to the dashed red spectra of sample IV (λ =1.87) can be discerned. The main difference appears in reduced Z'' values at frequencies below 10 kHz. This is due to the reduced thickness and the increased geometric capacitance of the stronger stretched sample.
The diagrams of Fig. 3-6(c) and (d) show the real and imaginary impedance spectra of sample VI with stretch ratio λ=2.12 for different dwell times of the sample in water. With growing dwell time the spectra changes noticeably.
Figure 3-6(d) shows most prominent the appearance of the low frequency relaxation peak at ca. 50 mHz. The appearance of the low frequency relaxation peak allows to fit the data with an equivalent lumped circuit model shown in Fig. 3-7. The circuit model is based on some fundamental physical realities. The model describes the impedance of the VHB membrane with a parallel connection of a capacitance, C_m, and a resistance, R_m, which represent the geometric capacitance and the resistance of the membrane respectively. The membrane is contacted via the water column inside the test cell, and the series resistance of the water column is represented by the lumped resistive element R_c. The electrodes of the test cell contribute to the overall impedance with a small cell-capacitance C_c. With increasing dwell time of the VHB membrane in water, the water will be adsorbed by the VHB membrane and ions become detrapped and mobile; they can gradually move through and across the membrane.

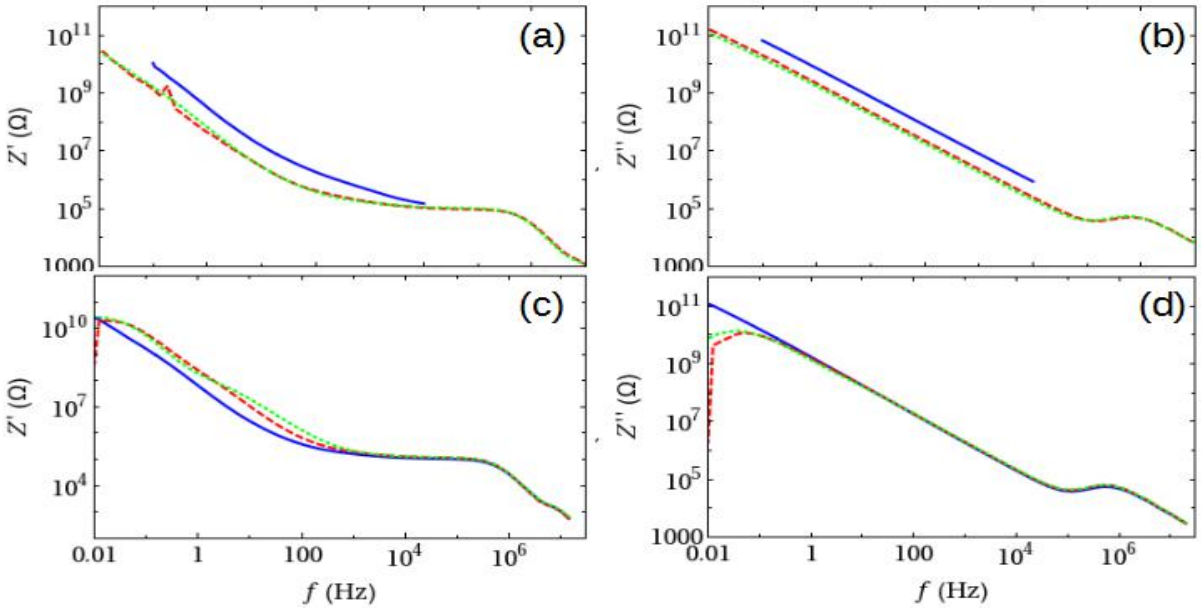

FIGURE-3-6 REAL PART (A) AND IMAGINARY PART (B) OF THE IMPEDANCE OBTAINED FROM 0.5 MM THICK VHB MEMBRANES WITH STRETCH RATIOS OF Λ=1 (SOLID BLUE) Λ=1.87 (DASHED RED), AND Λ=2.12 (DOTTED GREEN), ALL MEASURED RIGHT AFTER FIRST CONTACT WITH WATER.
REAL PART (C) AND IMAGINARY PART (D) OF THE IMPEDANCE OBTAINED FROM 0.5 MM THICK VHB MEMBRANES WITH A STRETCH RATIO OF Λ=2.12 AFTER A DWELL TIME IN WATER OF 0 H (SOLID BLUE), 2 H (DASHED RED) AND 24 H (DOTTED GREEN).

The mobile ions cause an additional capacitance, C_i, due to ionic double layer formation at the membrane/water interfaces. Alternating fields at low frequencies cause a redistribution of these ions, and the resistance against such a redistribution is described with an ion related resistor R_i.

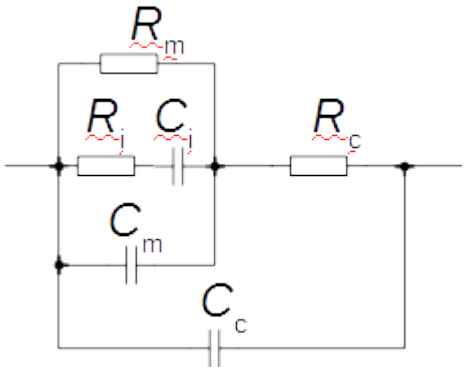

FIGURE-3-7 EQUIVALENT LUMPED CIRCUIT MODEL FOR THE IMPEDANCE OF THE EXPERIMENTAL ARRANGEMENT WITH A VHB MEMBRANE INSTALLED TO THE WATER FILLED TEST CELL.

This results in a frequency dependent polarization of the membrane which can be described by a distributed Debye relaxation function. With the incorporation of a distributed Debye relaxation into the lumped circuit model the total capacitance of the VHB sample is expressed by

(1)

The frequency dependent capacitance, with the angular frequency $\omega=2\pi f$, is a complex function where the imaginary unit is expressed with $i=\sqrt{(-1)}$, and the exponent β describes the distribution width of relaxation processes. With this frequency dependent capacitance the impedance of the VHB sample is

(2)

The exponent α is an experimental parameter frequently used with dielectric impedance models. It describes spatial variations of R_m and C_m and its influence on the distribution of the ionic relaxation processes. With Eq. (1) and Eq. (2) the overall impedance of the model is described with

(3)

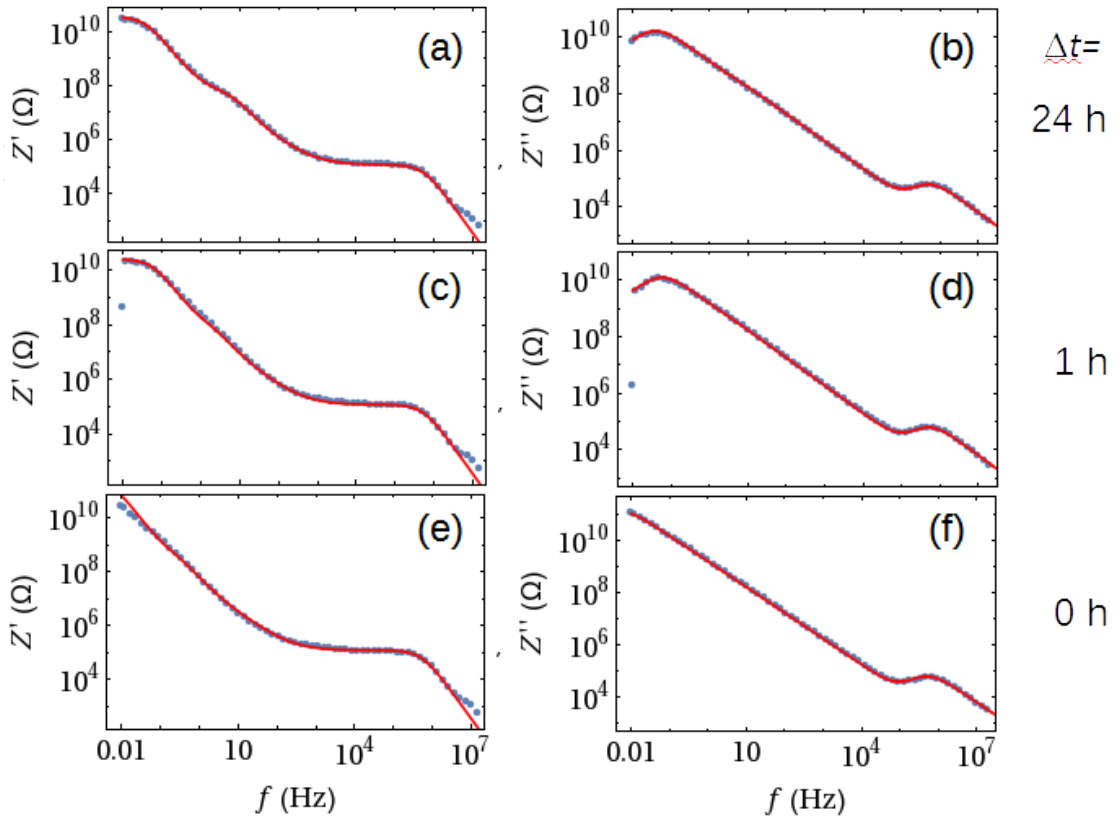

FIGURE-3-8 EXPERIMENTAL DATA (BLUE DOTS) AND MODEL CALCULATIONS (RED LINE) OF THE IMPEDANCE RELATED TO A 0.5 MM THICK VHB MEMBRANE WITH A STRETCH RATIO OF Λ=3 FOR DIFFERENT DWELL TIMES, ΔT, IN WATER.

This model function has been fitted to the impedance data of sample VI for all three measurements at different dwell times. The calculated fit functions and their agreement with

the experimental data are shown in Fig. 3-8. The main features of the experimental impedance are well described by the model. In particular the relaxation between 0.2 Hz and 200 Hz, which is well visible after a dwell time of 24 h (Fig. 3-8(a) and (c)), could be modelled exclusively with the distributed Debye relaxation function and the associated sample capacitance given with Eq. (1). The fitting process was first performed with the data that had been obtained from the last measurement with the longest dwell time of 24 h. This data set shows all relaxations sufficiently expressed and unique fit parameters could be determined. The fit parameters for shorter dwell times were obtained by slight variations of the previous values. All fit parameters are listed explicitly in Tab. 2-1. The cell related parameters R_c and C_c were kept constant at all fitting processes. Both parameters are exclusively responsible for the high frequency Z''-peak at ca. 500 kHz. Also the geometric capacitance of the membrane, C_m, remained unaltered.

The most important variations of parameters are associated with the ion polarization and the ion motion in the membrane. The relevant parameters are plotted versus dwell time in the diagrams of Fig. 3-9. The dc resistance of the membrane, R_m, shown in Fig. 3-9(a), decreases by one order of magnitude within a dwell time of less than one hour, and it remains at a level of about 28 GΩ. This is a rather low value for a material that is supposed to block charge migration effectively, and it is thus one important reason for the fast charge decay which was presented and discussed in section 2.1, *Charge decay*.

TABLE 3-1. FIT PARAMETER OF THE IMPEDANCE MODEL FOR A STRETCHED (Λ=2.12) VHB MEMBRANE IN WATER WITH DIFFERENT DWELL TIMES.

Δt (h)	✔	🚲	R_m (GΩ)	C_m (pF)	R_i (GΩ)	C_i (pF)	R_c (kΩ)	C_c (pF)
0.2	0.990	0.999	250	10	94.00	5.8	124	2.45
2.0	0.990	0.990	25	10	9.08	9.0	124	2.45
24.0	0.984	0.985	32	10	1.50	20.0	124	2.45

A further important observation shown in Fig. 3-9(b) is the continuous decrease of the resistance, R_i, against the ion motion and the simultaneous increase of the ion related capacitance, C_i, shown in Fig. 3-9(c). Both parameters explain exclusively the growing relaxation that is visible in the Z' values with growing dwell time of the sample in water. The time evolution of the ion related fit parameters indicate a steadily increasing amount of adsorbed water in the VHB membrane. The adsorbed water increases the effective permittivity of the material, as plotted with Fig. 3-9(d), and it further allow both extrinsic and intrinsic charge carriers to move with increasing efficiency within the membrane. The respective ion relaxation time, $\tau_i = R_i C_i$, is plotted versus dwell time with the diagram in Fig. 3-9(d); it decreases from about 0.54 s down to 30 ms. With the increasing dwell time of the membrane in water the diversity of ion relaxation processes also increases and the distribution of relaxation times broadens. This is indicated by the continuous decrease of the β-parameter plotted in Fig. 3-9(e).

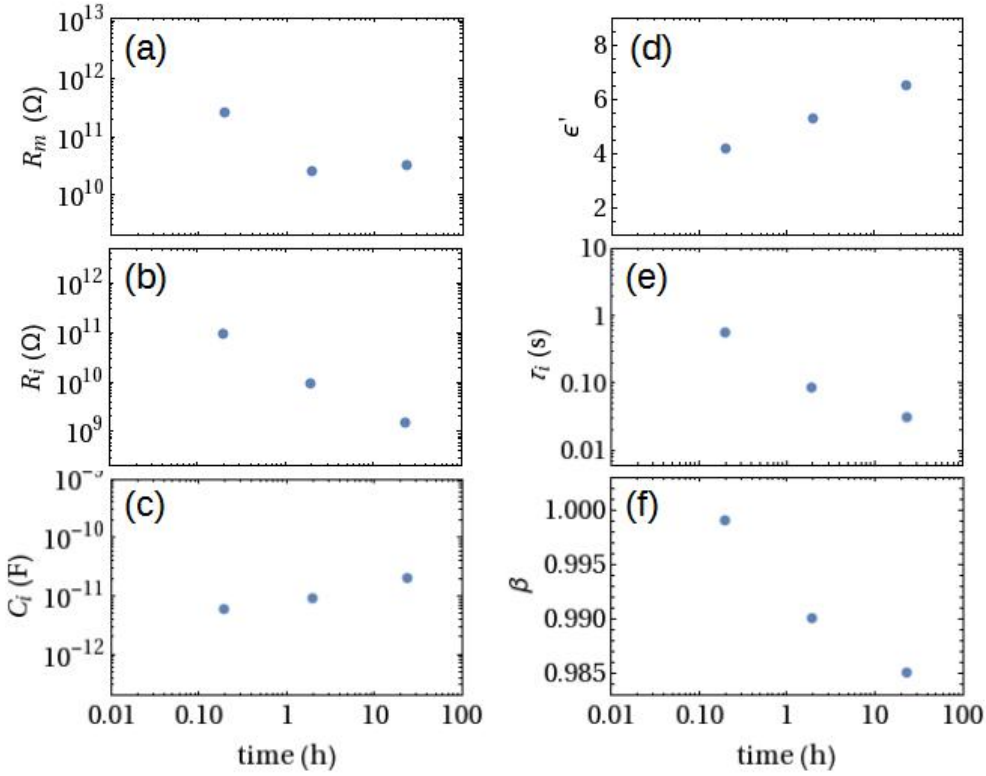

FIGURE-3-9 FIT PARAMETERS ASSOCIATED WITH ION MOBILITY AND ION POLARIZATION INSIDE THE STRETCHED (Λ=2.12) VHB MEMBRANE FOR DIFFERENT DWELL TIMES IN WATER.

The extent of the water induced degradation of the dielectric properties can be anticipated, if the experimental impedance data, Z' and Z'', are transformed in the equivalent representation of an effective parallel resistance, $R_p=(Z'^2+Z''^2)/Z'$, and parallel capacitance, $C_p=-Z''/(Z'^2+Z''^2)$. The diagram in Fig. 3-10(a) compares the green dotted R_p values of the 111 µm thick (t_n=0.5 mm and λ =2.12), and 24 h water soaked VHB sample,

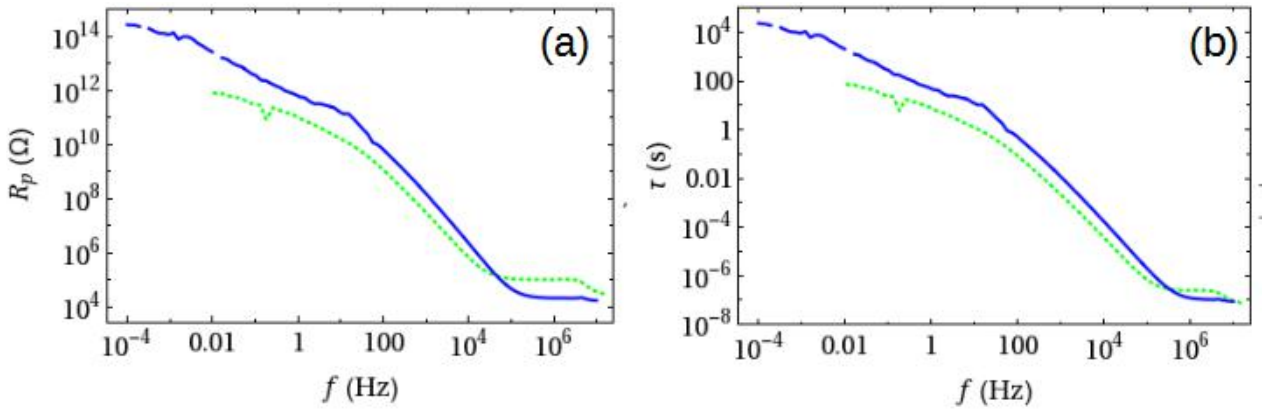

FIGURE-3-10 EFFECTIVE PARALLEL RESISTANCE (A) AND THE THICKNESS INDEPENDENT TIME CONSTANT (B) OF A 25 µM THICK PTFE (SOLID BLUE) AND A 111 µM THICK VHB MEMBRANE WITH A STRETCH RATIO OF Λ=2.12 (DOTTED GREEN).

With the R_p values of a 25 µm thick PTFE foil, which has been measured right after the installation to test cell. The PTFE is an excellently insulating dielectric which provides a high charge storage stability. The related low frequency R_p values are more than two orders of

magnitude larger then the R_p values of the water soaked VHB. The diagram shown in Fig. 3-10(b) compares the thickness independent time constants, $\tau=Z''/Z'$. Also this comparison shows a difference by more than two orders of magnitude.

Dielectric breakdown

Extensive dielectric breakdown measurements were conducted with VHB membranes of various stretch ratios. The breakdown strength was tested both with carbon grease electrodes in air, and without electrodes in water. The experiments with water were done with the test cell introduced in Fig. 3-1. For both methods the electric field in the membrane was increased with a voltage ramp at a rate of 50 V/s. The breakdown voltage recorded was the maximal voltage before the current through the membrane exceeded the 0.2 mA limit of the high voltage source. The results of the dielectric breakdown measurements with VHB membranes are given in the diagram of Fig. 3-11. All VHB

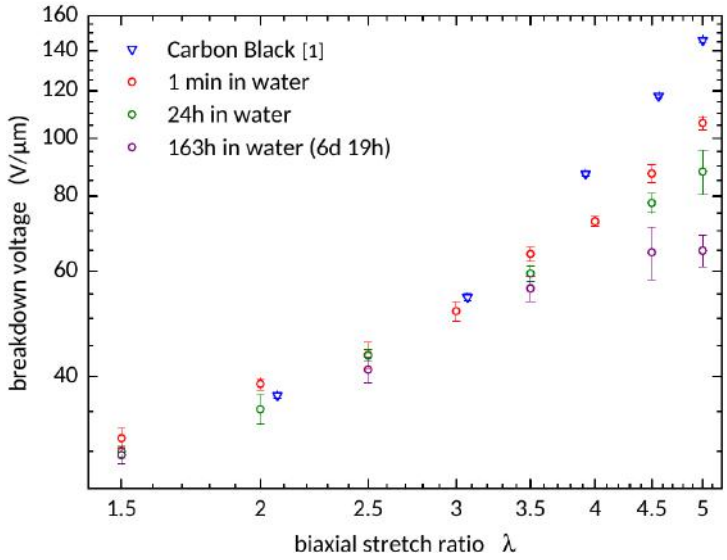

FIGURE-3-11 BREAKDOWN VOLTAGE VS. STRETCH RATIO OF VHB MEMBRANES IN AIR WITH CARBON GREASE ELECTRODES AND IN WATER MEASURED AT DIFFERENT DWELL TIMES WITHOUT ELECTRODES.

membranes tested had a nominal thickness of t_n=1 mm. Every stretch ratio was repeatedly measured with 3 to 10 new samples for the error bar statistics. The diagram shows a general increasing breakdown strength with increasing stretch ratio. The diagram shows also that the breakdown strength decreases with growing dwell time of the samples in water. The dwell time related decrease is more pronounced for VHB samples with larger stretch ratios. The dielectric breakdown strength of VHB in water reduces moderately for stretch ratios λ <3. For large stretch ratios, λ >3.5 the reduction in breakdown strength is much more significant, especially for samples with increased dwell time. It can thus be concluded, that the adsorbed water in the VHB dielectric reduces the dielectric strength of the elastomer. The effect is more pronounced for samples with large stretch ratios because the dc resistance, as discussed above, is greatly reduced.

Summary VHB

In summary, the performed experiments with the VHB elastomer (charge decay, dielectric impedance spectroscope and dielectric breakdown measurements) under various conditions

showed that the application of a bare VHB in water can't be utilized for a waterbased DEG. The data analysis of the experimental results allowed to explain the insufficient properties in terms of adsorbed water which strongly reduces the resistivity for both extrinsic and intrinsic migrating charges. Any material or any combination of materials that are suitable for a membrane of a waterbased DEG need significantly improved water repellent properties.

Natural rubber

The natural rubber materials "ZruElast A1040" and "Oppo Band 8003" were investigated for their usability as harvesting membranes of waterbased DEGs. "ZruElast A1040" (from Zrunek Gummiwaren GmbH) is a 300 µm thick natural rubber sheet containing 23wt% of inorganic fillers and 1.19 wt% of carbon. "Oppo Band 8003", from Oppo Medical Inc., is a 227 µm thick rubber sheet containing 0.96 wt% inorganic fillers and 0.56 wt% carbon. The properties of both materials are very similar. The majority of experiments were performed with "Oppo Band 8003", and the results are summarized below.

Charge decay

The natural rubber "Oppo Band 8003" with a thickness of 227µm was installed to the test cell and charge decay measurements were performed as described above in section 1.1. Figure 2-12 shows the drop of the normalized voltage over time. The data of the first measurement are plotted with a solid blue line and the data of the successive second

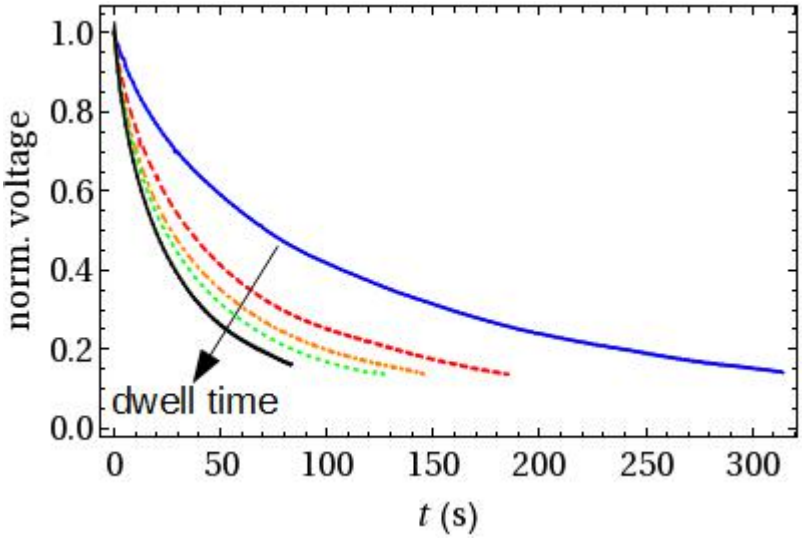

FIGURE-3-12 NORMALIZED VOLTAGE DROP DUE TO CHARGE DECAY OF 300 µM THICK NATURAL RUBBER MEMBRANE MEASURED IN WATER WITHOUT ELECTRODES AFTER A DWELL TIME OF ~30 S (SOLID BLUE), 350 S (DASHED RED), 550 S (DOT-DASHED ORANGE), 700 S (DOTTED GREEN), AND 1500 S (SOLID BLACK).

measurement are plotted with a dashed red line. The dwell time of the sample in water at the start of the second measurement was about 350 seconds. This duration is sufficient to cause a pronounced reduction of the charge stability. With growing dwell time the charge stability reduces further as it is illustrated with the plotted voltage drops of the 3rd, 4th, and 8th measurements. The 8th measurement, plotted with a solid black line, started after a dwell time

of ca. 1500 seconds. During this period the half-life time of the charges has reduce from t_{50}=72 s to t_{50}=20 s. These values are clearly better than those obtained with the VHB membranes. However, the data of Fig. 3-12 expose natural rubber as a rather unstable material whose dielectric properties are noticeably affected by water. The extent to which water affects the dielectric nature of natural rubber was investigated with dielectric impedance spectroscopy.

Impedance spectroscopy

Various samples of natural rubber "Oppo Band 8003" were prepared with different stretch ratios, λ, and mounted to the test cell. Impedance measurements were performed within different time intervals, Δ*t*. The listing below gives an overview over the tested natural rubber samples:

- sample I λ = 1, Δ*t*={0.2 h, 0.9 h. 2.5 h. 3.2 h,4.4 h, 22.4 h}
- sample II λ = 1, Δ*t*={0.2 h. 1 h, 2 h, 3 h, 4 h, 5.3 h, 23 h}
- sample III λ = 1.4, Δt={ 0.2 h,1 h, 1.8 h, 2.9 h, 19.4 h}
- sample IV λ = 1.4, Δ*t*={0.2 h,1 h, 2.4 h, 3.5 h, 4.4 h, 5.3 h, 24 h}
- sample V λ = 2.24, Δ*t*={0.2 h, 0.8 h, 2 h, 3 h, 17.6 h}
- sample VI λ = 2.24, Δ*t*={0.2 h, 1 h, 1.8 h, 2.9 h, 3.8 h, 25 h}

The following will present and discuss a selection of important result. The diagrams in Fig. 2-13(a) and (b) shows the real part, *Z*',and the imaginary part, *Z*'', of the impedance spectra of sample I versus the frequency *f*. The solid blue line is the first sample impedance measured right after the installation to the test cell. With growing dwell time of the sample in water the impedance decreases continuously. After a dwell time of about 22 h the real part has dropped to the low level of 1 MΩ which is less than one order of magnitude above the resistive value of the water column inside the test cell: Essentially this means that the 227 µm thick natural rubber has become conductive. It is instructive to transform the impedance data into the equivalent representation of an effective parallel resistance and a parallel capacitance, C_{p}. Figure 3-14(a) shows the evolution of the effective parallel capacitance with growing dwell time. At the low frequency of *f*=10 mHz the Cp value grows by five orders of magnitude. This drastic increase indicates a strong increase of mobile ionic carriers which in turn increases the loss tangent, tanδ, as presented in Fig. 3-14(b). A closer analysis shows that the increase in capacitance, which is due to the increase of the permittivity, can be well explained by the theory of electrode polarization due to mobile ionic carriers.

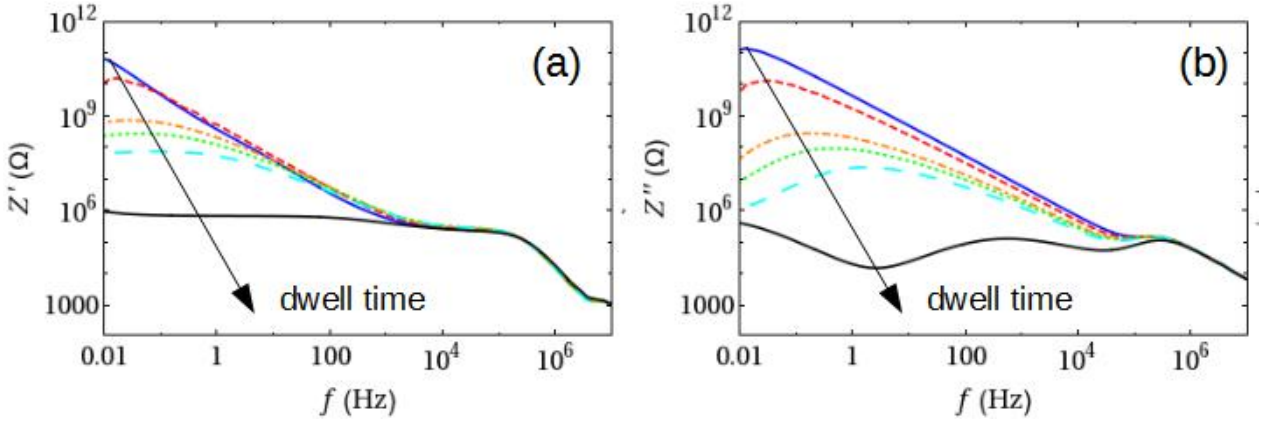

FIGURE-3-13 IMPEDANCE SPECTRA OF A 227 µM THICK NATURAL RUBBER MEMBRANE IN WATER. THE DIAGRAMS SHOW THE REAL (A) AND THE IMAGINARY (B) PART OF THE IMPEDANCE WHICH WERE MEASURED AFTER DWELL TIMES OF 0.2 H (SOLID BLUE), 0.9 H (DASHED RED), 2.5 H (DOTDASHED ORANGE), 3.2 H (DOTTED GREEN), 4.4 H (LARGE DASHED CYAN), AND 22.4 H (SOLID BLACK)

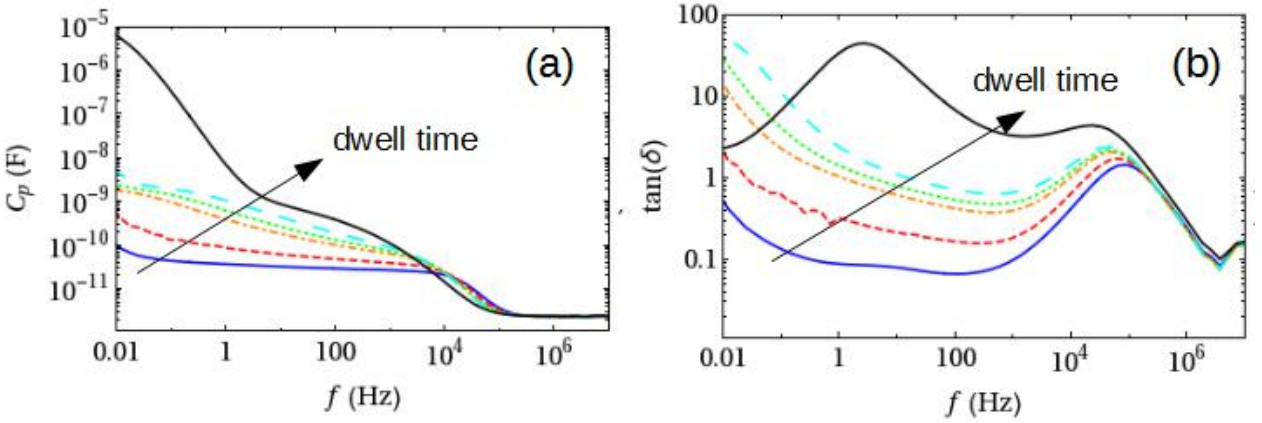

FIGURE-3-14 EXPERIMENTAL CAPACITANCE (A) AND LOSS FACTOR (B) CALCULATED FROM THE IMPEDANCE SPECTRA OF A 227 µM THICK NATURAL RUBBER MEMBRANE IN WATER. RESPECTIVE MEASUREMENTS WERE PERFORMED AFTER DWELL TIMES OF 0.2 H (SOLID BLUE), 0.9 H (DASHED RED), 2.5 H (DOTDASHED ORANGE), 3.2 H (DOTTED GREEN), 4.4 H (LARGE DASHED CYAN), AND 22.4 H (SOLID BLACK).

Thus, it can be concluded, that the natural rubber "Oppo Band 8003" contains a considerable amount of ionic species which become highly mobile if a sufficient amount of water is adsorbed. This observable effect is suppressed to a large extent, if the rubber material is stretched. The diagrams in Fig. 3-15(a) and (b) show the measured impedance of sample VI which had been stretched to a ratio of $\lambda = 2.24$. Similar to the spectra of stretched VHB samples the Z' part of the impedance changes only moderately in a low frequency window between 100 mHz and 10 Hz.

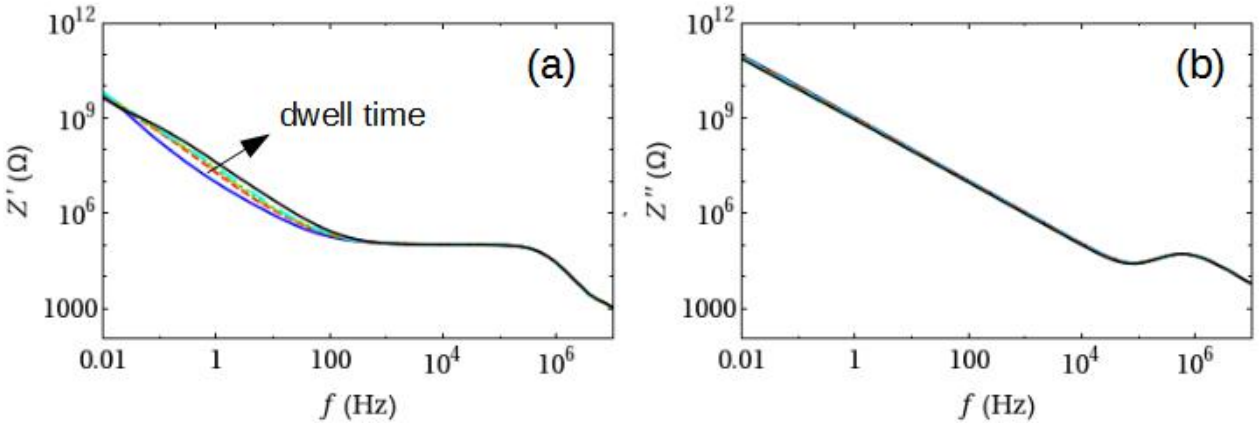

FIGURE-3-15 IMPEDANCE SPECTRA OF A STRETCHED (λ=2.24) NATURAL RUBBER MEMBRANE IN WATER. THE DIAGRAMS SHOW THE REAL (A) AND THE IMAGINARY (B) PART OF THE IMPEDANCE WHICH WERE MEASURED AFTER DWELL TIMES OF 0.2 H (SOLID BLUE), 0.9 H (DASHED RED), 3.2 H (DOTTED GREEN), 4.4 H (LARGE DASHED CYAN), AND 22.4 H (SOLID BLACK).

The stretched rubber cannot adsorb as much water as the relaxed rubber does. The stored elastic energy barrier is too high and prevents any strong volume increase necessary for water adsorption. Only few ionic carriers are detrapped.
Despite the moderate effect of water on the dielectric properties of the stretched material, the important insulating parameters, the effective parallel resistance, R_p, and the thickness independent time constant, τ, are both almost identical to the respective values of VHB. This can be seen in Fig. 3-16(a) and (b) which compares the respective values of PTFE (solid blue line) and the λ = 2.24 stretched natural rubber after 0.2 h (dashed red line) and after 25 h (dotted black line) dwell time in water.

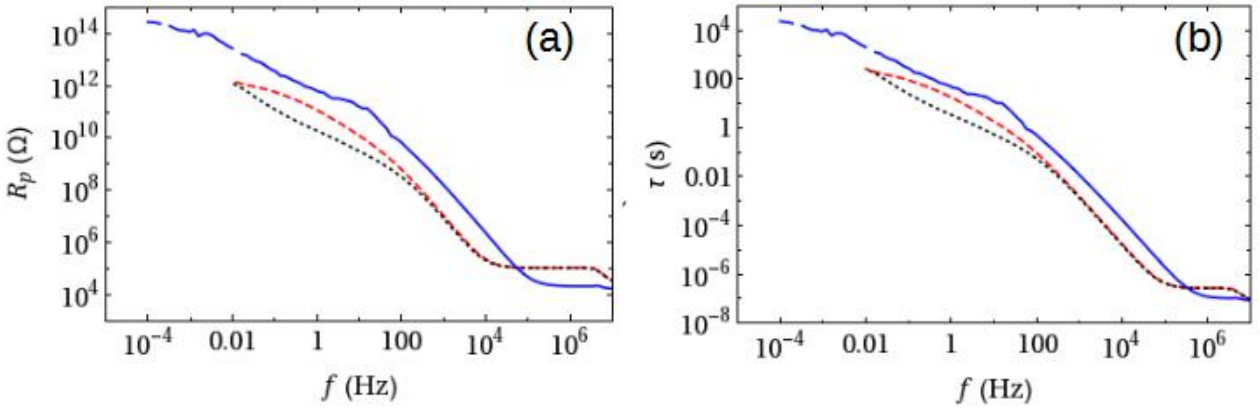

FIGURE-3-16 EFFECTIVE PARALLEL RESISTANCE (A) AND THE THICKNESS INDEPENDENT TIME CONSTANT (B) OF A 25 µM THICK PTFE (SOLID BLUE) AND A 45 µM THICK NATURAL RUBBER MEMBRANE WITH A STRETCH RATIO OF Λ=2.24 MEASURED IN WATER AFTER A DWELL TIME OF 0.2 H (DASHED RED) AND 25 H (DOTTED BLACK).

3.2 Electrodes

3.2.1 Bare water electrode

Bare water electrodes can be used only with membrane materials or systems which show a high degree of hydrophobicity. As discussed in section 2.1 the simple bulk materials, VHB and

natural rubber, were found to be too absorbent for water making them too conductive for migrating charges and thus inappropriate for any application with bare water electrodes. Elastomer materials with a much improved hydrophobicity might be found within the polymer class of fluoroelastomers like Viton. The investigation of this material will be one of the next steps in this project.

3.2.2Water repellent surface modification

In order to improve the water repellent properties of the elastomer membranes first experiments were conducted with oil-treated VHB surfaces. Figure 3-17 presents diagrams with low frequency impedance spectra of two VHB membranes, both with a stretch ratio of λ=2.6. The spectrum of the membrane which was treated with silicon oil is plotted as dashed red line. The spectrum of the untreated membrane is plotted as solid blue line for comparison. It is immediately evident that the oil treated VHB has a much reduced resistivity.

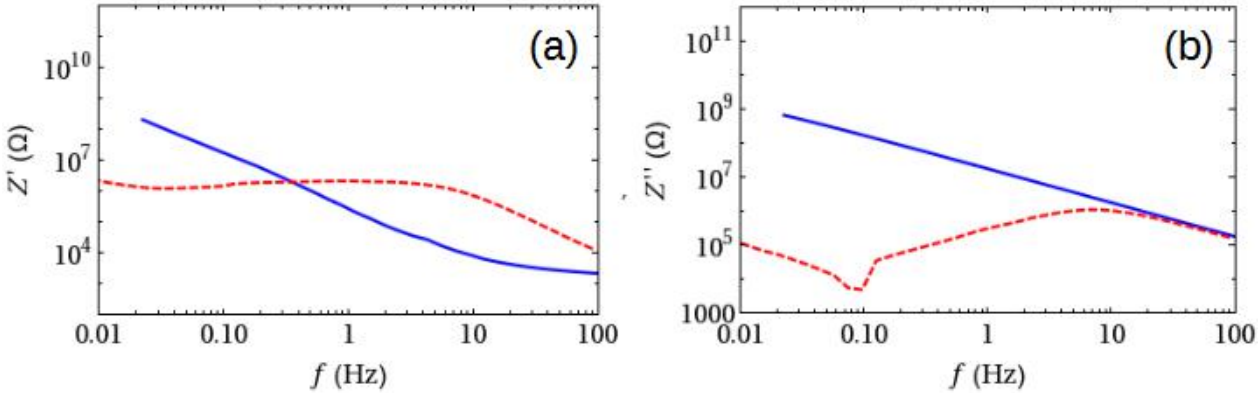

FIGURE-3-17 IMPEDANCE SPECTRA OF STRETCHED (λ=2.6) VHB MEMBRANES IN WATER. THE REAL (A) AND THE IMAGINARY (B) PART OF THE IMPEDANCE WERE MEASURED WITH AN UNTREATED (SOLID BLUE) VHB MEMBRANE, AND WITH AN OIL TREATED (DASHED RED) VHB MEMBRANE.

The real part of the impedance has reduced by more than three orders of magnitude (from $>10^9$ to $\sim 10^6$ Ohms). This result was found also with other oils and greases and also with natural rubber. The reason for this contra intuitive result is currently unknown. All elastomer membranes were tested with oil-containing carbon grease electrodes, and no negative effects were observable. Oil alone does not affect the dielectric properties of elastomer membranes. Oil in combination with water however, damage the insulating properties significantly.

3.2.3 Hydrogel electrode

A salt water filled hydrogel was fabricated out a 2 mm thick polyacrylamide hydrogel sheet. An emulsion of ethyl cyanoacrylate glue and trimethylpentane (1:10) was used to bond two 2mm thick polyacrylamide hydrogel discs (19mm diameter) to both sides of a circular VHB 4910 elastomer. Ethyl cyanoacrylate (Loctite 406, Henkel) was used as bonding agent. The bonding occurs within seconds as the water in the hydrogel accelerates the polymerization process of the ethyl cyanoacrylate. Therefore, the bonding can be instantly loaded.

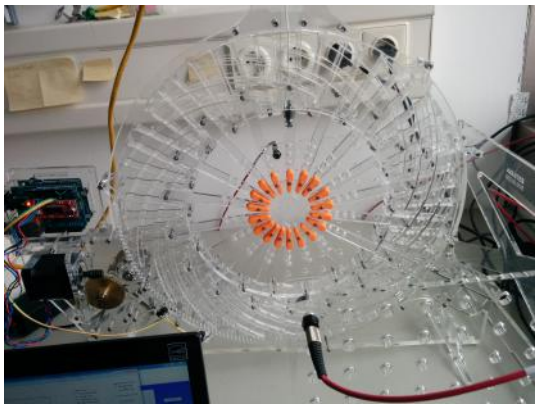

FIGURE-3-18 RADIAL STRETCH SYSTEM FOR THE STRETCHING OF VHB ELASTOMERS WITH BONDED HYDROGEL ELECTRODES.

Impedance spectroscopy

The disk shaped VHB 4910 elastomer with the bonded hydrogel electrodes was mounted to a radial stretch system, which is presented in Fig. 3-18. The 18 fingers of the stretch system stretched the VHB-hydrogel membrane successively in 27 equidistant steps of $\Delta\lambda$=0.16 to a final stretching ratio of λ=4.4. Impedance spectra were recorded for every single stretch ratio. A summary of the impedance data for three different stretch ratios (1, 2.1, and 4.4) is given with the diagrams of Fig. 3-19. The diagram in Fig. 3-19(a) shows the effective parallel resistance which indicates a membrane resistance larger than 10^{12} Ohms. The effective time constant, plotted with the diagram of Fig. 3-19(b) shows values of >16 s for a frequency of f=1 Hz. These parameters are clearly better compared to the respective values obtained with VHB and bare water electrodes (f=1 Hz, λ=2.12: Rp= 4.6 10^{10}, τ=4.2).

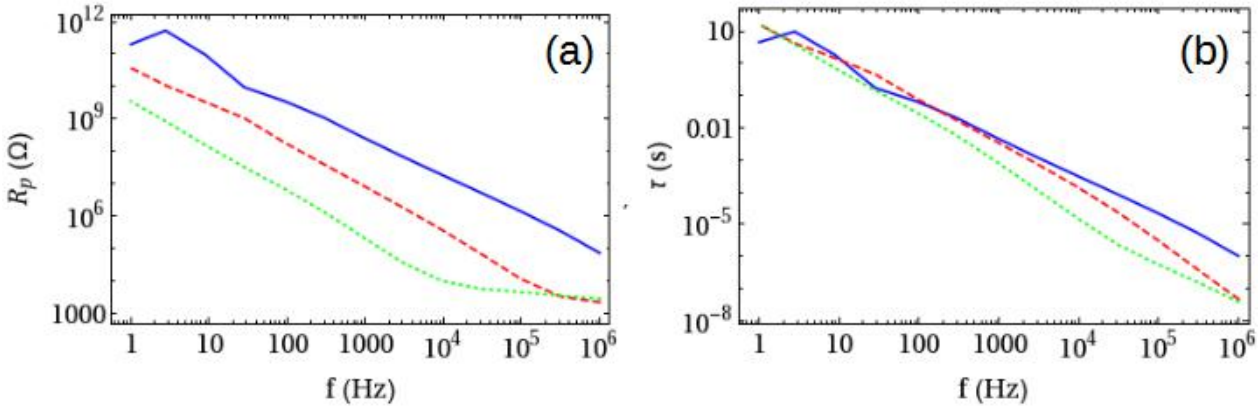

FIGURE-3-19 EFFECTIVE PARALLEL RESISTANCE (A) AND THE THICKNESS INDEPENDENT TIME CONSTANT (B) OF A VHB MEMBRANE WITH HYDROGEL ELECTRODES AT STRETCH RATIOS OF Λ=1 (SOLID BLUE), Λ=2.1 (DASHED RED), AND Λ=4.4 (DOTTED GREEN).

Energy harvesting, experimental setup and result

Because of the promising impedance spectra, a hydrogel-elastomer system was prepared for an energy harvesting experiment. The schematic outline of the experiment is shown in Fig. 3-20(a). The hydrogel-VHB membrane is mounted on a buffer chamber of volume 350 cm^3 and is deformable by air pressure and voltage. The inflation of the hydrogel-VHB membrane allows for equal-biaxial stretch in the top region. Due to inflation, the area of the hydmembrane

expands and the thickness decreases, so that the capacitance of the membrane increases. The mechanical energy flows are monitored by tracking the excess pressure, p, in the chamber and the volume, V, of the inflated balloon-like hydrogel-VHB membrane with a video system. Two charge reservoirs of different voltages, U_{in} and U_{out}, are realized by using high-voltage capacitors with capacitive values much larger than the maximum capacitance of the membrane. The voltage of the hot hydrogel electrode, U_m, is measured without electrical contact by a Kelvin probe voltmeter (TREK model 341 A) to avoid charge leakage through the measurement instrument. The hydrogel electrode of the inflating membrane is connected to the output reservoir when the measured voltage, U_m, has reached the voltage of the output reservoir. Further inflation cause a slight increase in the voltage ΔU_{out} of the output reservoir which determines the amount of charge stored

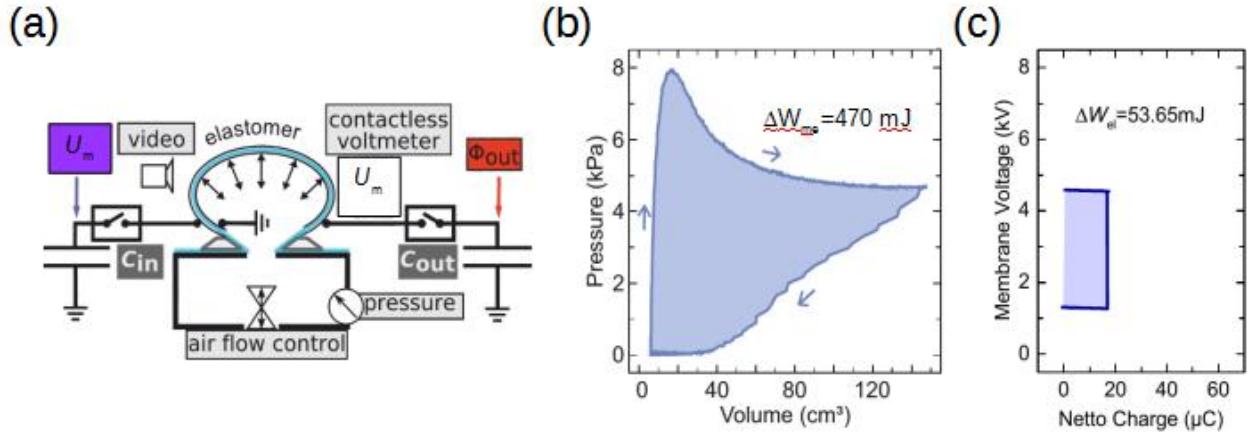

FIGURE-3-20 SCHEMATIC OF THE EXPERIMENTAL TEST STAGE TO MEASURE THE MECHANICAL AND ELECTRICAL ENERGY FLOW IN A DIELECTRIC ELASTOMER GENERATOR MEMBRANE. (A) MECHANICAL WORK CONJUGATE PRESSURE/VOLUME GRAPH MEASURED WITH HYDROGEL ELECTRODES, (B) AND THE CORRESPONDING ELECTRICAL WORK CONJUGATE VOLTAGE/CHARGE GRAPH. (C)

to the output reservoir, $\Delta Q = C_{out} \Delta U_{out}$. A similar procedure determines the charge drawn from the input reservoir. Figure 3-20(b) depicts the clockwise path of the DEG cycle in the (p, V) plane. The enclosed area corresponds to a mechanical work of W_{me}=470 mJ used in the conversion process. The evolution of the electrical parmeters can be seen in Fig. 3-20(c). The enclosed area in the (U, Q) plane results in a corresponding electrical energy of ca. 54 mJ. The mechanical to electrical energy conversion efficiency of the hydrogel-VHB membrane calculates to ca. 11.5 %.
This fairly large conversion efficiency is an encouraging result and suggests further research in the improvement and development of even better hydrogel electrodes.

3.3 Encapsulation

3.3.1 VHB sandwich structure

First charge decay experiments as discussed in section 2.1, were conducted with sandwiched VHB membranes. A schematic of such a membrane is sketched in Fig. 3-21.

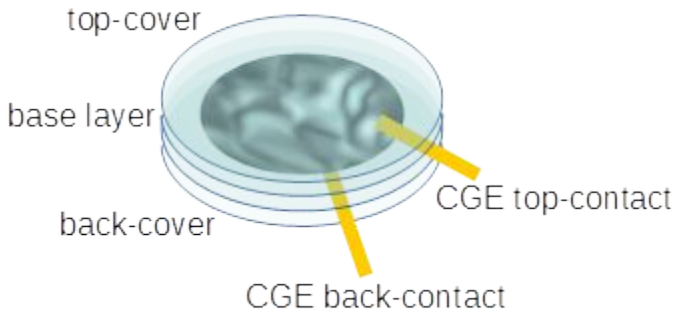

FIGURE-3-21 VHB SANDWICH STRUCTURE CONSISTING OF A MIDDLE LAYER WITH TWO CARBON GREASE ELECTRODES ON BOTH SIDES JACKETED BY TOP- AND BACK-COVER LAYERS.

A central VHB foil serves as base layer with carbon grease electrodes on both sides. The electrodes are contacted via thin copper stripes. The top and the back are both covered by two further VHB foils. The sandwiched system was installed to the test cell and successive charge decay measurements were performed as described above in section 2.1. Figure 3-22(a) shows the drop of the normalized voltage over time. The first measurement of the unstretched VHB sandwich, plotted with a solid blue line in the diagram of Fig. 3-22(a) was conducted in air. The second and the third measurement, plotted with dashed red and dotted green liens, were performed with the unstretched VHB sandwich structure submerged in water. Both measurements gave identical results. This suggests that at least for a dwell time of more than 700 s water has not soaked through the VHB cover layers. Further more, the recorded data indicate that after t_{50}=36 seconds 50 % of the charge has decayed. In comparison to the decay time measured with bare VHB membranes the charge decay time of the VHB sandwich structure has increased by more than a factor of 3.8. This indicates an improvement in stability with respect to charge decay and water resistance. Because of this encouraging result the charge decay properties of the VHB sandwich had been tested further in a stretched configuration. The VHB sandwiched used in the previous experiment was stretched to a ratio of ca. λ =3.6 and charge decay measurements were performed again.

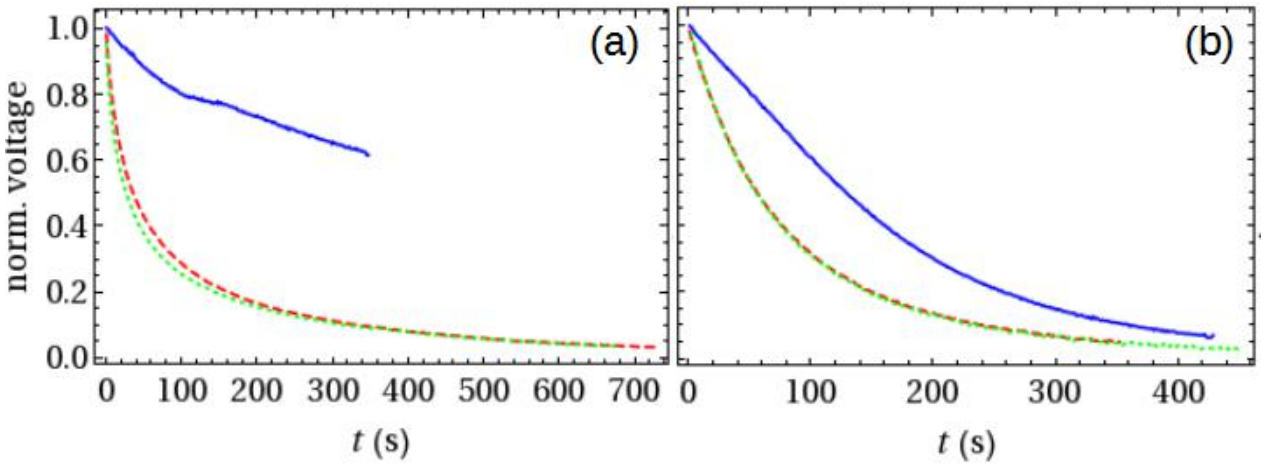

FIGURE-3-22 NORMALIZED VOLTAGE DROP DUE TO CHARGE DECAY OF A RELAXED (A) AND A Λ=3.3 STRETCHED (B) VHB SANDWICH STRUCTURE MEASURED IN WATER AFTER A DWELL TIME OF ~30 S (DASHED RED), AND AFTER 750 S (DOTTED GREEN). THE FIRST MEASUREMENT IN AIR (SOLID BLUE) IS PLOTTED FOR COMPARISON.

The related data of three successive measurements are plotted in the diagram of Fig. 3-22(b). The solid blue line shows the decreasing voltage versus time of the first measurement. After the elapsed time of t_{50}=131 seconds 50 % of the charge has decayed. This is a further improvement in charge stability compared to the unstretched VHB sandwich. This is general feature of VHB elastomers which show improving dielectric properties with increasing stretch ratio. The next two measurements however show that this result cannot be maintained and the charge decay occurs at a faster rate with increasing dwell time of the sandwich system in water. The normalized data of the successive second decay measurement, plotted as dashed red line, reveals a much faster charge decay. The t_{50} time has reduced to ca. t_{50}=57 s. Presumably, in the course of the first measurement, during the dwell time of more than 400 s, water penetrated through the stretched top- and back-cover layers and also through the central base layer which reduced the insulating properties. However, compared to the dwell time related results obtained from the bare VHB membranes, the charge stability of the VHB sandwich structure is better by more than a magnitude. A further encouraging result is the fact that the rate of degradation is also slowed down considerably: For a bare VHB membrane with a dwell time in water for about 290 s between the first and the last measurement, Fig. 3-2 shows an ongoing decrease of the t_{50} time from 10 s down to ca. 6 s. For the VHB sandwich structure Fig. 3-22(b) after a dwell time for about 800 s the t_{50} time between the second and third measurement has not changed and remains still at 57 s. This degradation stability is a direct result of the increased membrane thickness which significantly reduces the water concentration gradient across the VHB sandwich membrane. Consequently the diffusion driven adsorption of water is reduced notably. These results show a much improved charge stability compared to bare bulk membranes, and they also indicate a real potential of such encapsulated membrane systems for a successful utilization as central element in waterbased DEGs. Follow-up experiments will investigate and demonstrate energy harvesting with further improved encapsulated membrane systems.

4. MANUFACTURING PROCEDURES

4.1 Introduction to manufacturing issues

The core sub-system of a DEG is the elastomeric unit that is composed by alternative layers of conductive and dielectric deformable materials. For the CD-DEG it consists in a stack of circular elastomeric sheets that are pre-stretched and clamped along their perimeter.

As highlighted in Deliverable 2.3, the implementation of effective DEGs in the range of 10-100kW for WECs requires the industrial production of large size membranes (in the range 20-80 m^2, i.e. 4-9m in diameter) that are made of highly deformable materials (up to 200-300%). These membranes must have a multilayer structure in which conductive layers are alternately stratified (and eventually bonded) with dielectric layers. Eventually, the external faces of the membrane-assembly could be covered by a passive/watertight layer that acts as a barrier against water seepage (see Section 3).

A first issue was the identification of suitable materials for both dielectric and conductive layers. A lot of work has been done to find appropriate dielectric materials, less effort has been spent for the study of conductive layers.

Identified dielectric materials that provide promising performances are: silicones elastomers, acrylic rubbers, natural rubbers and styrene based rubbers (see Section 2).
For the conductive layers, the more mature technology is based on silicone materials [6]. Conductive silicone based layers can be coupled with strong/reliable bonding with silicone dielectric layers. (this is the technique that is considered the most promising for first pre-commercial dielectric elastomer transducers). Silicone conductors can be also coupled to other dielectric materials (such as acrylics or natural rubber) but the lack of strong bonding may lead to problems on the long term. However, this last problem is mitigated in the case of the CD-DEG since loading mode is contributing to avoid delamination of layers.
Conductive layers to be coupled with natural and synthetic rubbers have been recently studied and some very promising results have been obtained with metal sputtering (see Section 2), that is a process that could be potentially scaled up to industrial production through roll-to-roll sputtering techniques But this last solution still needs to be investigated in depth.

4.2 CD-DEG Modular layout/architecture

The CD-DEG membrane is composed of a stack of dielectric/conductive elastomeric layers that are foreseen to be arranged according to the modular architecture that is schematically represented in Figure 1. Specifically, the DEG-PTO is composed by q modules and each module consists of a n-layered DEG membrane that is driven by its independent driving electronics.

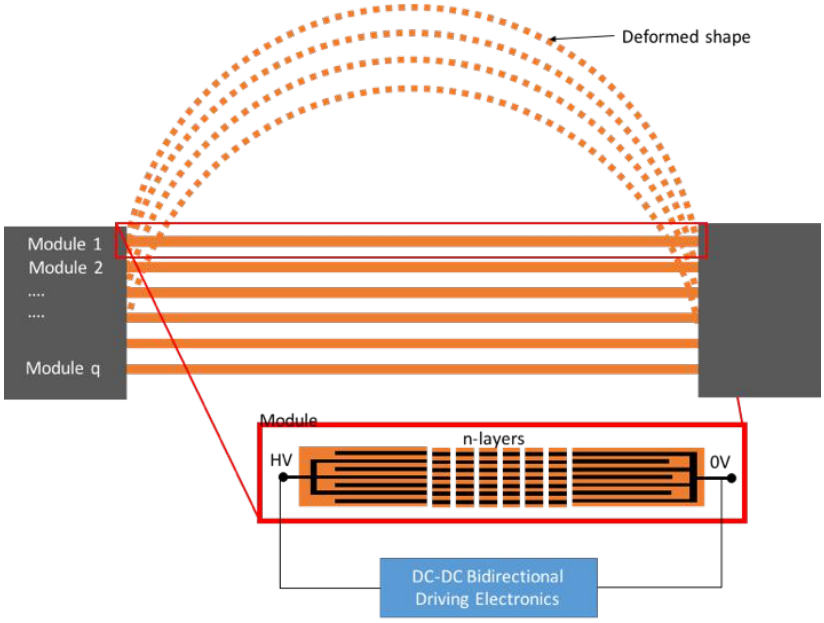

FIGURE-4-1: SCHEME OF THE MODULAR ARCHITECTURE OF THE DEG-PTO.

The choice of this architecture is driven by the following motivations:

- Adaptability: modules can be combined in different numbers so as order to match the different specifications of the several types of WEC that could employ the considered DEG-PTO;
- Reduction of the mean time to maintenance and increase in availability: the eventual problems for the failure due to electrical breakdown of the dielectric layers of one of the membranes are confined only to the interested module without compromising the functionalities of the whole WEC system.
- Simplified Manufacturing and reduced costs: cost advantage could be determined by economy of scale by producing the same components that can be adapted to several different WECs.

Given the relatively immature stage of development of DEG technology, the commercialization roadmap has been initially drafted according to a gradual approach. Specifically, the architecture of the final high-power DEG-PTO system illustrated in Figure 4-1 could be obtained through four sequential progressive steps. This is the route that is suggested to prosecute DEG-PTO development and to finally make it a commercial product.

4.3 Identification of technological Gaps

There are appropriately mature industrial procedures for producing silicone elastomer membranes at relatively small scales. Wacker Polymers is commercializing A4 sheets and rolls with widths up to 30cm that have been purposely developed for dielectric elastomer transducers applications. These solutions can be employed (with limited effort) for implementing also larger scale prototypes for research purposes. However, these materials are currently too expensive and it is not really clear how (and if) mass production could reduce their costs.

Rubbers such as Natural Rubber (NR) or Styrene Rubber (SR) are much more promising from the point of view of costs but manufacturing procedures for the whole composite structure (dielectric + conductive layers) are still undefined.
Research should be oriented to the understanding on how existing industrial processes could be adapted (or redesigned) for the manufacturing of DEGs based on NR or SR.

1) Solutions for producing large membranes (range of 20-80m^2):
To produce large assemblies of alternating layers of dielectric and conductive materials two approaches are currently prospected:

a. Single continuous process: the final assembly of alternating conductive and dielectric layers is obtained in a single continuous process.
b. Two stage production and bonding: the final assembly of alternating conductive and dielectric layers is obtained via a two phases process in which dielectric and conductive layers are produced independently (first phase) and bonded subsequently (second phase).

The first approach is likely to be more effective but requires a major effort for its development, the latter approach is more feasible in the short term but less effective from the economical point of view. Reliable/scalable solutions have to be conceived to bond conductive layers with dielectric layers. Silicone conductive layers can be coupled with strong/reliable bonding with silicone dielectric layers but, as previously mentioned, for these materials there are some concerns regarding economic feasibility.
For other materials, research efforts are still needed to understand material combinations and bonding methodologies.

Other alternatives for the implementation of industrial processes include:

a. Develop industrial plants that have to be adapted (or redesigned) to produce very large sheets of rubber with high accuracy in the thickness of dielectric and conductive layers that need to be properly bonded together. Possible problems: dimensions of calender cylinders, the produced dielectric (and conducting) layers should have small thicknesses (100-500 microns) with small error tolerances (1-3%).
b. Produce smaller area membranes (that can be produced with current technologies) and use techniques for soldering them into larger assemblies. Possible issues: soldering joints must be as deformable/compliant as the rest of the membrane since they are subjected to the same mechanical loading cycles.

5. CONCLUSIONS

This deliverable reports on first activities conducted within the work-package 5 of the WETFEET project that are aimed at studying and advancing the technology of Dielectric Elastomer Generators (DEG) for PTO of wave energy converters.
Specifically, in this first phase of the project the activities have focussed on:

- testing and modelling material properties in dry conditions;
  Several key material properties of elastomeric materials that are employed for implementation of DEG-PTO have been analysed in the past but further aspects were still to be analysed such as leakage losses due to residual conductivity of insulators, joule losses due to residual resistivity of conducting materials, and possible detrimental effect on material properties due to water contact.
  In the first phase of the activities of WP5 (Task 1), the focus was set on the study on those aspect of material choice and combination that were not previously investigated. Specifically, a comprehensive study on the insulation properties of dielectric materials and the conductivity of materials employed for electrodes have been introduced. The most promising materials have been considered for the dielectrics (acrylic elastomers, natural and synthetic rubbers) and electrodes (filled PDMS, crumpled metalized electrodes).
  Absolute values for conductivity have been measured and preliminary projections have been made in order to understand the effect of these properties on real scale devices.
  It has been concluded that materials such as silicone and rubbers possess the insulation qualities to be employed has dielectric materials for DEGs. Acrylic elastomers are less reliable and presents high batch to batch variability. This could be attributable to manufacturing issues. Actually, material films that are tested are mostly conceived for completely different applications and their performance could be improved by assuming tailor-made manufacturing procedures. For what concern materials for electrode it has been found that solutions that employs composite silicone-carbon black materials can achieve a sufficient level of conductivity, i.e. the power loss during the required charging and discharging cycles are estimated to be well below 1%.

- testing materials in wet/submerged conditions;
  The acrylic elastomer VHB and natural rubber are two materials which are known to be highly appropriate for the fabrication of electroactive membranes in the dry environment. The suitability of these materials for water powered elastomer generators, where the membrane will be in direct contact with water, was unexplored and has been investigated. Comprehensive measurements of charge stability, dielectric strength, and dielectric impedance spectroscopy showed an unfavorable effect of water on the dielectric properties and the charge stability of the materials. Neither VHB nor natural rubber can be applied in a simple arrangement as electroactive membrane if operated in direct contact with water. Promising results however, were obtained with more elaborate compound multilayer systems. An energy-harvesting experiment could be performed successfully with an hydrogel/VHB compound. The obtained mechanical-to-electrical conversion efficiency was 11.5 %. This marks a substantial improvement in comparison to bare VHB membranes.

Experiments with VHB showed that water has a deteriorating effect on the electrostatic charge stability of the elastomer. The half life time of stored charges reduced from about 20 seconds in air to ca. 9 seconds in water and it drops further with increasing dwell time in water. After a dwell time of 400 seconds the half life time has already reduced to just about 6 seconds. This time scale is too short for any efficient energy harvesting cycle. An explanation for this degradation was found with impedance spectroscopy: The elastomer adsorbs water, and water mobilizes extrinsic and intrinsic charges in the bulk and on the surface of the material. The mobility of charges increases with increasing dwell time of the material in water.
The effect of water induced charge mobility was found to be even more pronounced in natural rubber. After a dwell time of less than 24 hours the resistance of a 300 µm thick rubber sheet with a diameter of 15 mm has reduced from several giga-ohms to less than 800 kohms. The natural rubber under investigation contains a considerable amount of charge carriers which become highly mobile if a sufficient amount of water is adsorbed.
The obtained results suggest to shield the dielectric elastomer from the adverse effects of water by protecting barrier layers. A promising approach was found with 2 mm thick salt water hydrogel layers. The hydrogel is elastic and has a twofold advantage: it withholds the water from the dielectric elastomer by the osmotic pressure and it is conductive. The hydrogel layers thus serve as direct electrodes for the dielectric membrane. In a similar manner the dielectric membrane can be shielded with additional elastomer layers. Experiments with a VHB membrane and carbon grease electrodes sandwiched between two extra VHB layers showed also promising results. The half life time of stored charges remained at a stable value of about 50 seconds even after dwell times of ca. 5000 seconds.
The successful experiments with hydrogel and sandwich multilayer systems are setting the perspective for further research and development work. The water barrier properties of hydrogel layers will be carefully scrutinized and tested for their long term stability at various water pressure. In addition, new flour- and silicone elastomer materials with supposedly better water resistance will be examined for their applicability as electroactive membrane and as barrier layers.

- defining full-scale layout and architecture of the DEG-PTO:
  A preliminary analysis is provided on manufacturability of full scale DEG-PTO main components. A general layout/architecture for the full scale DEG-PTO is proposed according to a modular structure that make it possible to simplify/improve several issues. Possible existing manufacturing technologies are identified for the development of full-scale systems up to a scale of tens of kilowatts. However, the need of innovative manufacturing technologies is also identified for the development of larger scale systems. A gradual roadmap for the development is sketched.

BIBLIOGRAPHY

[1] Moretti, G., Rosati, G. P. P., Alves, M., Grases, M., Vertechy, R., & Fontana, M. (2015, May). Analysis And Design of an Oscillating Water Column Wave Energy Converter with Dielectric Elastomer Power Take-Off. In ASME 2015 34th International Conference on Ocean, Offshore and Arctic Engineering. ASME.

[2] Vertechy, R., Rosati, G. P. P., & Fontana, M. (2015). Reduced model and application of inflating circular diaphragm dielectric elastomer generators for wave energy harvesting. Journal of Vibration and Acoustics, 137(1).

[3] Vertechy, R., & Fontana, M. (2015). Electromechanical characterization of a new synthetic rubber membrane for dielectric elastomer transducers. In SPIE Smart Structures and Materials+ Nondestructive Evaluation and Health Monitoring . International Society for Optics and Photonics.

[4] Foo, C. C., Cai, S., Koh, S. J. A., Bauer, S., & Suo, Z. (2012). Model of dissipative dielectric elastomers. Journal of Applied Physics, 111(3), 034102.

[5] Madsen, F. B., Yu, L., Mazurek, P., & Skov, A. L. (2016). A simple method for reducing inevitable dielectric loss in high-permittivity dielectric elastomers. Smart Materials and Structures, 25(7), 075018.

[6] Rosset, S., & Shea, H. R. (2013). Flexible and stretchable electrodes for dielectric elastomer actuators. Applied Physics A, 110(2), 281-307.

[7] Ong, H. Y., Shrestha, M., & Lau, G. K. (2015). Microscopically crumpled indium-tin-oxide thin films as compliant electrodes with tunable transmittance. Applied Physics Letters, 107(13), 132902.

[8] Beck, J. V., Cole, K. D., Haji-Sheikh, A., & Litkouhi, B. (1992). Heat conduction using Green's functions. Washington DC: Hemisphere Publishing Corporation.

[9] Rosset, S., Araromi, O. A., Schlatter, S., Shea, H. R. Fabrication Process of Silicone-based Dielectric Elastomer Actuators. *J. Vis. Exp.* (108), e53423, doi:10.3791/53423 (2016).

[10] Kaltseis, R., Keplinger, C., Koh, S. J. A., Baumgartner, R., Goh, Y. F., Ng, W. H., ... & Bauer, S. (2014). Natural rubber for sustainable high-power electrical energy generation.

[11] S. J. A. Koh, C. Keplinger, T. Li, S. Bauer and Z. Suo, "Dielectric Elastomer Generators: How Much Energy Can Be Converted?," in *IEEE/ASME Transactions on Mechatronics*, vol. 16, no. 1, pp. 33-41, Feb. 2011.

[12] Vertechy, R., Fontana, M., Papini, G. R., & Forehand, D. (2014, March). In-tank tests of a dielectric elastomer generator for wave energy harvesting. In *SPIE Smart Structures and Materials+ Nondestructive Evaluation and Health Monitoring* (pp. 90561G-90561G). International Society for Optics and Photonics.

[13] Vertechy, R., Rosati, G. P. P., & Fontana, M. (2015). Reduced model and application of inflating circular diaphragm dielectric elastomer generators for wave energy harvesting. *Journal of Vibration and Acoustics*, *137*(1), 011004.

[14] Righi, M., Vertechy, R., & Fontana, M. (2014, September). Experimental Characterization of a Circular Diaphragm Dielectric Elastomer Generator. In

ASME 2014 Conference on Smart Materials, Adaptive Structures and Intelligent Systems (pp. V001T03A013-V001T03A013). American Society of Mechanical Engineers.

[15] G. Moretti, G. P. P. Rosati, M. Fontana and R. Vertechy, "Hardware in the loop simulation of a dielectric elastomer generator for oscillating water column wave energy converters," *OCEANS 2015 - Genova*, Genoa, 2015, pp. 1-7.

[16] Moretti, G., Rosati, G. P. P., Alves, M., Grases, M., Vertechy, R., & Fontana, M. (2015, May). Analysis And Design of an Oscillating Water Column Wave Energy Converter with Dielectric Elastomer Power Take-Off. In *ASME 2015 34th International Conference on Ocean, Offshore and Arctic Engineering* (pp. V009T09A023-V009T09A023). American Society of Mechanical Engineers.

[17] B. Teillant et al.; Techno-economic comparison between air turbines and dielectric elastomer generators as power take off for oscillating water column wave energy converters; EWTEC Conf.; Nantes; 2015

[18] R. Vertechy ; M. Fontana; Electromechanical characterization of a new synthetic rubber membrane for dielectric elastomer transducers. Proc. SPIE 9430, Electroactive Polymer Actuators and Devices (EAPAD) 2015, 94300K (April 1, 2015).

[19] R. Vertechy ; M. Fontana ; G. Stiubianu ; M. Cazacu; Open-access dielectric elastomer material database. Proc. SPIE 9056, Electroactive Polymer Actuators and Devices (EAPAD) 2014, 90561R (March 8, 2014)